

PPPL- 4588

PPPL-4588

## 23rd IAEA Fusion Energy Conference: Summary Of Sessions EX/C and ICC

R.J. Hawryluk

January 2011



# Princeton Plasma Physics Laboratory

## Report Disclaimers

---

### Full Legal Disclaimer

This report was prepared as an account of work sponsored by an agency of the United States Government. Neither the United States Government nor any agency thereof, nor any of their employees, nor any of their contractors, subcontractors or their employees, makes any warranty, express or implied, or assumes any legal liability or responsibility for the accuracy, completeness, or any third party's use or the results of such use of any information, apparatus, product, or process disclosed, or represents that its use would not infringe privately owned rights. Reference herein to any specific commercial product, process, or service by trade name, trademark, manufacturer, or otherwise, does not necessarily constitute or imply its endorsement, recommendation, or favoring by the United States Government or any agency thereof or its contractors or subcontractors. The views and opinions of authors expressed herein do not necessarily state or reflect those of the United States Government or any agency thereof.

### Trademark Disclaimer

Reference herein to any specific commercial product, process, or service by trade name, trademark, manufacturer, or otherwise, does not necessarily constitute or imply its endorsement, recommendation, or favoring by the United States Government or any agency thereof or its contractors or subcontractors.

---

## PPPL Report Availability

### Princeton Plasma Physics Laboratory:

<http://www.pppl.gov/techreports.cfm>

### Office of Scientific and Technical Information (OSTI):

<http://www.osti.gov/bridge>

---

### Related Links:

[U.S. Department of Energy](#)

[Office of Scientific and Technical Information](#)

[Fusion Links](#)

# **23rd IAEA Fusion Energy Conference: summary of sessions EX/C and ICC**

R. J. Hawryluk

Princeton Plasma Physics Laboratory, PO Box 451, Princeton, NJ 08543, USA

Email: rhawryluk@pppl.gov

## **Abstract:**

An overview is given of recent experimental results in the areas of innovative confinement concepts, operational scenarios and confinement experiments as presented at the 2010 IAEA Fusion Energy Conference. Important new findings are presented from fusion devices worldwide, with a strong focus towards the scientific and technical issues associated with ITER and W7-X devices, presently under construction.

## **1. Introduction**

An impressive collection of recent experimental results in the areas of innovative confinement concepts, operational scenarios and confinement experiments were presented at the 2010 IAEA Fusion Energy Conference. Ten papers on innovative confinement concepts, 28 on operational scenarios of stellarators, ELMy H-mode discharges and advanced operating modes, and 51 on confinement experiments addressing energy transport and turbulence, particle transport, rotation and momentum transport, and L-H transition and pedestal physics were presented at this conference. In this paper, important new findings are summarized from fusion devices worldwide, with a strong focus towards the needs of the major next step fusion experiments, ITER and W7-X. With such a wide-ranging selection of topics, this paper has concentrated on those results, which have more general import, and all papers have not been summarized. The results described here rely on an extensive literature, which, in general, is cited within the references of the papers summarized here but not subsequently referenced here.

## **2. Innovative Confinement Concepts**

At this conference, the heading of innovative confinement concepts included a broad range of configurations and topics with some related papers in the confinement session: levitated dipoles [1,2], field reversed configurations [3,4], mirror machines [5-8], spheromaks [9], helical-tokamak hybrid [10], magneto-inertial fusion [11], current amplification by helicity injection [12,13] and direct energy conversion [14] as well as construction or upgrades of research facilities [15-17]. A couple of examples will be highlighted to illustrate the breadth of research reported at the conference.

Observation and analysis of magnetospheric plasmas indicates that low-frequency fluctuations drive inward diffusion of trapped particles, creating centrally peaked density and temperature profiles. This is simulated in laboratory levitated dipole experiments [1,2]. When the dipole is

levitated in the Levitated Dipole Experiment (LDX) centrally-peaked density profiles result, plasma confinement improves, and a strong inward particle pinch is inferred to maintain a relatively fixed shape of the density profile [1]. This is shown in figure 1, in which the applied electron cyclotron heating (ECH) power is modulated to vary the density but the ratio of the two density interferometer channels is approximately constant indicating that the shape is not changing. The strong central peaking of the density is inferred to be due to an inward turbulent pinch, since the ionization source occurs primarily in the outer regions of the plasma. Experiments on the levitated dipole, Ring Trap 1 (RT-1), have also observed peaked density profiles when the supports for the dipole were removed. Improved high- $\beta$  ECH plasmas have been obtained on RT-1 by the optimization of plasma formation operation and by compensation of the geomagnetic field. The maximum local  $\beta$  value reached 70%, and particle confinement time is approximately 0.6 s in the most recent experiments in RT-1. The plasma pressure is mainly due to the hot electrons and peaks in the strong field region [2].

Neutral beam injection has been a mainstay heating system of the mirror machine, tokamak and stellarator programs for nearly four decades and is now being applied to the field reversed configuration (FRC). The theoretical motivation for neutral beam injection into a FRC is, in part, to stabilize MHD instabilities by the presence of an energetic particle population. In the TS-4 device, shown in figure 2, the field-reversed configuration is attained by merging two spheromaks. Hydrogen beam with energy of  $\sim 13$  keV and current of  $\sim 5$  A is tangentially injected to the argon FRC plasma formed by counter-helicity merging. Figure 2 shows that neutral beam injection decreases the decay rate of the FRC plasma. The reduction in the energy decay rate is much larger than expected from the increased NBI power of  $\sim 65$  kW alone, suggesting that global stability of the FRC is improved by the neutral beam injected fast ions [4].

The promise of achieving parameters suitable for a fusion materials neutron source, has motivated the development of the gas dynamic trap. The key concept is that a population of fast ( $\sim 100$  keV) ions is created by oblique injection of neutral beams. The maximum density of the sloshing ions is at the turning point, where the peak fusion neutron production would occur. An electron temperature of 750 eV will be required for a fusion neutron source, while with the existing power of 6MW  $\sim 200$  eV has been achieved. Figure 3 shows recent measurements of the magnetic field indicating that  $\beta \approx 60\%$  has been achieved [5].

While parallel confinement has historically been a major issue for the development of the mirror concept, experiments on GAMMA 10 have also studied radial confinement, which can also affect performance. The installation of additional electron cyclotron power together with measurements of potential fluctuations using a gold heavy ion beam probe and of density fluctuations has enabled the study of how electron cyclotron power affects radial transport. The electron cyclotron power is applied to the plug and called P-ECH in figure 4 increasing the potential and creating a positive electric field. The radial particle flux is calculated from the measured phase difference between the potential and density fluctuations. The application of P-ECH is correlated with a significant reduction in the radial particle flux [8].

### **3. Operating Scenarios**

The extension of operating scenarios and the development of control techniques to modify those scenarios, which were described in the discussion of innovative confinement concepts, is also evident in the papers on stellarators, tokamaks, spherical tori, and reversed field pinches offering the promise of further optimization of the various configurations. The development and refinement of the operational scenarios provides a strong foundation for the initial operation of the next generation of large fusion facilities, ITER [16] and W7-X [17], which are under construction.

### 3.1 Stellarator Operating Scenarios

The achievement of transient super dense core (SDC) densities up to  $1 \times 10^{21} \text{ m}^{-3}$  by means of pellet injection in LHD has been previously demonstrated. These results have been extended by means of multiple pellet injection to sustain a high core density as shown in figure 5. There is a slow degradation in confinement time, which is associated with enhanced recycling, increasing the edge neutrals and resulting in a radiation collapse. The peaked density profile has central densities  $\sim 2\text{-}3 \times 10^{20} \text{ m}^{-3}$ . The region designated as the super dense core is characterized by good particle confinement. In these discharges, the large Shafranov shift modifies the edge topology. In the region outside of the internal diffusion barrier (IDB), particle diffusion in the edge mantle is much greater and can be further enhanced by resonant magnetic field perturbations. As shown in figure 6, the resonant magnetic field perturbations result in a reduction in density in the mantle and increased central density. This is qualitatively similar to observations in several tokamak experiments though whether the underlying physics is the same remains to be determined. The IDB-SDC regime can be achieved with either a local island or a helical divertor. The relatively rapid transport in the mantle region also results in decreasing impurity accumulation, which is critical for sustainment [18].

The increase of ECH power on LHD enabled the extension of peak electron temperatures and the study of electron- Internal Transport Barriers (e-ITB). The highest electron temperatures in excess of 15 keV and the steepest profile were obtained for a magnetic configuration with  $R_{\text{axis}} = 3.53 \text{ m}$ , which is predicted to be the optimum condition with respect to the predicted neoclassical transport. A clear density threshold (and/or  $P_{\text{ECRH}}/n_e$  threshold) for the formation of the e-ITB was observed. The electron temperature profile drastically changed from flat to peaked when the density was reduced below the threshold and the radial electric field made a transition from negative to positive at the core region. Relative to the previous reported results of  $\sim 10 \text{ keV}$ , the achievement of 15 keV corresponds to a significant extension of operating space; however, it is important to note that this was accomplished in low density plasmas ( $n_e \leq 0.23 \times 10^{19} \text{ m}^{-3}$ ) [19].

### 3.2 Superconducting Tokamak Operation

The publications of the ITER Physics Basis [20] and Progress in the ITER Physics Basis [21], along with the subsequent review of the ITER design, have highlighted not only important scientific issues but also operational issues associated with a tokamak incorporating superconducting toroidal and poloidal coil systems. The results from KSTAR [22] and EAST

[23] tokamaks have made major contributions to resolving these issues. The presence of a continuous current in the toroidal field coils has motivated the development of ICRF, high frequency glow discharge cleaning and lithium wall coating techniques to condition the chamber walls [22-24]. Figure 7 shows, in addition to the ICRF antenna used to heat the plasma, a dedicated antenna to condition the vacuum vessel wall in EAST [23]. Due to the limitation of the vessel bakeout temperature on ITER to 200 C and the presence of potential graphite coatings from the carbon divertor targets, the development of wall conditioning techniques is especially important.

A ramification of a tokamak with superconducting poloidal field coils and a thick vacuum vessel is that the applied voltage during plasma breakdown and rate of rise of plasma current is, in general, less than in previous machines with copper coils. Plasma startup and control with relatively low applied voltage on EAST and KSTAR has been successfully demonstrated. Experiments on DIII-D [25], FTU [26] and KSTAR [22] have shown that ECH assisted breakdown and startup is beneficial. The benefits of applying lower hybrid waves during the current ramp have been demonstrated on EAST [23] and C-Mod [27]. In addition, the development of the startup scenario on KSTAR has had to compensate for eddy currents in the vessel and cryostat, which are up-down asymmetric, and stray fields from the ferromagnetic Incoloy 908 alloy used in the superconducting cable conduit. As shown in figure 8, the stray field varies with major radius. Consequently, these fields not only degrade the quality of the initial field-null but also adversely affect the control of the plasma position after breakdown occurs [22]. Interestingly, experiments on DIII-D with 1-1.2MW of ECH during the preionization and breakdown phase are observed to be less sensitive to the details of the magnetic null and its location [25]. It is encouraging that despite the technical challenges associated with superconducting tokamaks the development of plasma scenarios is going well and the lessons learned will facilitate the commissioning of ITER plasma operation.

### 3.3 Development of Operating Scenarios for ITER

While superconducting tokamaks address important issues for ITER operation, most of the development continues to be done on devices with copper coils. During the past campaign, JET has reestablished operation with a plasma current of 4.5MA, which is valuable to minimize the extrapolation to ITER. In general, the results show plasma performance similar to that achieved in previous JET experiments. Nevertheless, a confinement factor of  $H_{98(y,2)} \sim 1$  at  $I_p = 4.5$  MA could not be achieved as shown in figure 9. This is attributed to enhanced plasma-wall interactions, due to the increasing absolute ELM size as the plasma current is increased resulting in increased ablation of carbon co-deposited layers [28]. Above 3.5MA active ELM moderation is required and utilized as will be discussed later in this paper leading to a modest impact on the energy confinement time [29,30]. If a similar impact were observed on ITER, this would have significant consequences in the value of  $Q_{DT}$  and underscores the need to develop ELM mitigation or suppression techniques that minimize the degradation in the energy confinement time.

During the ITER design review, the need for additional data on the current rampup and rampdown phases was identified to refine and update the specifications for the poloidal field coil

system. Experiments on JET were performed in helium and compared with similar JET deuterium discharges and found that, with the exception of small differences in flux consumption, very little difference in plasma inductance were observed at the end of the current rise phase, supporting the non-nuclear phase of ITER operation with helium [31]. Good progress in experimental simulations of the ITER current rampdown phase was reported on JET [31], C-Mod [32] and DIII-D [25] in avoiding increased flux consumption from the central solenoid and large increases in plasma inductance by remaining in H-mode, applying additional heating, and decreasing the plasma elongation. The comparison of the results with models, used during the burn phase, is in progress and indicates that further work is required to improve the modeling of the startup phase.

### 3.4 Operating Scenarios with Impurity Seeding

The large anticipated divertor heat fluxes on ITER, especially those impinging on tungsten divertor targets, have motivated the development of impurity seeding techniques to reduce the heat flux. Significant progress was reported on AUG [33], C-Mod [34] and JET [35] in reducing the heat flux while retaining good quality H-modes. An improvement in energy confinement with nitrogen seeding is shown in figure 10, with values of  $H_{98(y,2)}$  exceeding the best values in carbon-dominated AUG discharges at the same density and collisionality [33]; however, low collisionality values achieved in previous campaigns are so far not accessible in the all-tungsten AUG. In similar experiments improvement in confinement was not obtained on C-Mod [34] and a 10% reduction in confinement was observed on JET [35]. In AUG, operation of ICRF heating with all tungsten plasma facing components is hampered by ICRF-related tungsten influxes. In contrast, the C-Mod group [34], also with an all-metal first wall (molybdenum), observed that seeding is highly compatible with the use of ICRF and, additionally, the operational reliability of the ICRF system was improved, although the seeding must be done in conjunction with boronization for good H-mode performance.

### 3.5 Empirical Studies of L to H transitions

A key design requirement for ITER is operation in H-mode with good confinement. ITER is projected to operate near the L to H power threshold during the high  $Q_{DT}$  burn phase. As is well known, there is substantial scatter in the database used to extrapolate the power threshold required for a transition from L to H-mode [36]. The scatter in the database appears to, among other things, indicate that several key parameters are not captured in the scaling relationships. New results on the power threshold requirements in support of the ITER non-nuclear phase using helium have been reported along with many other interesting results, which will be briefly summarized. As reported by experiments on DIII-D [37] and JET [38], the ratio in the power threshold between deuterium and helium operation is density dependent, ranging from 1.5-2 at low density to 1-1.5 at high density as shown in figure 11. In contrast to the power threshold scaling law, which increases with density, a minimum power threshold at an intermediate density is observed. This minimum value is different in deuterium and helium discharges. On NSTX, the threshold power in helium is 20 to 40% greater than in deuterium [40]. The results at this meeting help unify previous experimental results and put in perspective the AUG results presented at the last IAEA meeting by Ryter et al [40], who reported that the H-mode power threshold in deuterium and helium discharges are comparable and increase the confidence that

H-mode regimes will be achieved in ITER's non-nuclear phase.

The effect of magnetic field perturbations on the power threshold has been studied due to both long wavelength (low- $n$ ) and more localized field perturbations. Low  $n$  perturbations are observed to increase the power threshold by 50% on NSTX [39] and 80% on MAST [41]. The effect of RMP perturbations on DIII-D is observed to be even more complicated where a significant increase, up to a factor of about two, is observed to occur above a threshold perturbation field level in deuterium discharges [37]. This threshold level was not observed in helium plasmas in which the power threshold increased with coil current even at low coil currents. Furthermore, non-resonant low- $n$  perturbations of the same field strength resulted in a much smaller increase in the power threshold than was found for resonant fields. A localized magnetic field perturbation was used to simulate the ITER test blanket module by external coils on DIII-D. In those experiments, no significant change in the power threshold was observed [42].

Application of lithium coatings in NSTX have identified that changes in recycling conditions have a large impact on the power threshold, which increases with larger lithium depositions, as shown in figure 12 [39]. Changes in magnetic configuration, which may also affect plasma recycling, have also been observed to affect the power threshold. By increasing the major radius of the X-point, the plasma triangularity was decreased in NSTX and the power threshold was observed to decrease. In these experiments, the value of the toroidal field at the X-point location appears to be the key variable [39]. The power threshold is observed to also depend on the height of the X-point as shown on MAST [41] in figure 13 and also on DIII-D [37] consistent with earlier observations on JET. The power threshold with X-point height can increase by a factor up to 2.5 over the range studied in DIII-D.

While each of these results provides valuable experimental results, the net impact is to underscore that many variables remain unaccounted for in the empirical power threshold scaling relations used to extrapolate to ITER.

### 3.6 Advanced Inductive Regime

While ELMy H-mode operation remains the baseline operating scenario for ITER, additional operating regimes are being explored. The advanced inductive regime, which operates at lower current, is potentially attractive to achieve long duration pulses to facilitate ITER studies requiring high integrated neutron fluence [43,44]. In recent JET experiments, by ramping the current down prior to the main heating phase, values of  $H_{98(y,2)} \sim 1.3$  are achieved, a significant improvement relative to earlier data on JET [43]. While this improvement in confinement factor and the values of the fusion energy figure of merit,  $G = \beta_N H_{89p} / q_{95}^2$  from a number of devices [44], are encouraging, the extrapolation to ITER is not straightforward. Energy confinement time scaling does not appear to be simply described by H-mode scaling. In particular in comparison experiments between DIII-D and JET the results are better described by Bohm  $\rho^*$  scaling than by gyro-Bohm [45]. Observed core ion temperature gradients in JET exceed those predicted by gyrokinetic calculations that do not include rotation [43]. These results indicate that the plasma profiles are not stiff in the core and that stiffness could be reduced by rotation in regions of low magnetic shear as discussed in [46]. In addition, the results on DIII-D show a clear improvement with rotation [44]. Thus while improved confinement in the advanced

inductive regime has been observed on a large number of devices [44], it is necessary to conduct further joint comparative experiments which have normalized rotation rates and  $T_i/T_e$  ratios comparable to ITER, while scanning  $\nu^*$  to improve the extrapolation to ITER and to other fusion devices.

A key element in the progress in developing the advanced inductive regime is the ability to sustain values of the safety factor above unity in the core. Experiments on AUG and DIII-D indicate that the observed current diffusion is not consistent with standard neoclassical modeling taking into account predicted bootstrap and beam driven currents, in contrast to results on JET, which indicate that they are consistent [43]. An understanding of these differences would improve the extrapolation to ITER and clarify what localized current drive techniques are effective in obtaining an optimum safety factor profile.

### 3.7 Steady-state Operating Regimes

Another interesting example, which illustrates how relatively subtle changes in the neutral beam heating sources can result in different reversed shear states, is from comparison experiments between JET and JT-60U with internal transport barriers as shown in figure 14 [47]. In general, there was a reasonable match in dimensionless parameters except in the core rotation profile and the resulting density profile, which affected  $\beta$  and  $\nu^*$ . In JT-60U with less rotation, the density profile was very peaked and the q-profile was strongly reversed. As a consequence of the peaked density profile, the core bootstrap current density is more than five times higher in JT-60U compared to JET and the reversed magnetic shear configuration is self-sustained in JT-60U scenarios. A key element in these experiments is particle transport in the core resulting in the peaked density profiles. The authors infer, from gyrokinetic quasi-linear calculations with QuaLiKiz, that in the region of reversed shear TEM modes are stabilized leading to inward convection and peaked density profiles. The peaked density profiles then result in stabilization of the ITG modes and increased bootstrap current [47]. Other experiments on JET indicate that the improved confinement in the steady-state operating discharges is associated with improved core confinement and the development of internal transport barriers [48]. Experiments on DIII-D indicate that the pressure peaking factor, which affects the bootstrap current, decreases significantly with the value of the minimum safety factor in the core and is less at higher values of  $\beta_N$  [49]. While current experiments with dimensionally similar discharges have provided valuable guidance in developing operating scenarios for ITER, the results are clearly sensitive to many experimental parameters. Hence, the development and validation of predictive models that can decrease the scenario development time on ITER remains an important goal.

### 3.8 Alternative Operating Regimes: QH and I-mode

A recurring topic at this conference [16, 50] was the development of techniques to mitigate or suppress the heat flux from ELMs in ITER. Progress was reported on the development of operating scenarios with good H-mode confinement but reduced particle confinement in the edge resulting in ELM-free operation without the buildup of density and impurities, which has historically been detrimental in ELM-free operating scenarios.

The QH-mode has been extensively studied on DIII-D in which an edge harmonic oscillation is

observed to increase particle transport. Most of the results were achieved by means of counter injection, which is not a planned ITER operating scenario. Progress has been made to extend the operating space by taking advantage of a theoretical prediction of neoclassical toroidal viscosity (NTV) and experimental observations on DIII-D that a non-resonant perturbation in the edge applies a torque to the plasma in the edge region toward the neoclassical offset velocity, which for these cases is in the counter direction. The NTV torque from the non-resonant magnetic perturbation is used to maintain the QH-mode as shown in figure 15 even after the applied neutral beam torque is reduced to zero [51].

The I-mode for improved confinement mode on C-Mod is usually obtained by operating in the unfavorable  $\mathbf{B} \times \nabla \mathbf{B}$  direction (away from the active X-point). As is well known, this results in a higher power threshold for an H-mode discharge. The I-mode experiments are characterized as an operating regime with power input near but typically below the transition to a H-mode. These discharges possess an edge temperature barrier without an associated particle barrier as shown in figure 16 [52, 53], which may be due to increased particle transport from an edge instability. One issue is whether it is possible to reliably operate in the I-mode and not transition into the H-mode since the operating regimes can overlap in power. Further work is needed to understand the ramifications of the QH-mode, utilizing non-resonant magnetic perturbations, and the I-mode for ITER and whether they can be used to avoid the deleterious effects of ELMs.

### 3.9 Lithium Coatings, Limiters and Divertors

While a major emphasis of the meeting was related to issues associated with ITER, techniques to extend the operation of toroidal devices were presented, which do not directly apply to ITER. At this meeting, lithium coatings to the first wall and lithium coated limiters and divertor plates were used on a number of different machines including a number of different magnetic configurations, including tokamak, spherical tori, stellarator, and reversed field pinch [23, 26, 54-58]. The use of lithium has enabled improved confinement, higher density and more reliable operation. Results from FTU [56], NSTX [54,55] and TJ-II [58] reported up to ~50% enhancements in energy confinement time. Experiments on NSTX have combined the benefits of lithium wall coatings together with a transition to an enhanced pedestal H-mode resulting in values of  $H_{98(y,2)} \sim 1.7$  in figure 17, with roughly comparable improvements being due to the lithium deposition and the transition to the enhanced pedestal H-mode [55,59]. In NSTX, the lithium coatings were critical in enabling density control and the achievement of quasi-steady state conditions for durations greater than an energy confinement time in the enhanced pedestal H-mode. Typically, ELM-free H-mode operation was obtained on NSTX with lithium coatings. To avoid the buildup of carbon impurities and density, ELMs were triggered by the application of  $n=3$  magnetic perturbations [60]. FTU has obtained peaked density profiles at high density with a liquid lithium limiter as shown in figure 18 and densities 30% beyond the Greenwald density limit at high  $q$ . The peaked density profiles are correlated with the presence of a MARFE and a strong density gradient in the edge [56]. LTX is being commissioned to explore the use of liquid lithium wall coatings on a thick conducting segmented wall to improve plasma performance [61]. The extrapolation of these interesting results with lithium to steady state operating conditions and especially to operation with tritium remains to be established.

### 3.10 Operating Scenarios in Reversed Field Pinch Experiments

The reversed field pinch community reported progress in extending their operating range. As shown in figure 19, the central electron temperature has continued to increase with plasma current in RFX, which met its design current of 2MA. The increased electron heating and electron temperature at higher plasma current results in increased values of the magnetic Lundquist number, which was previously correlated with reduced internally driven tearing mode amplitude on MST and RFX [57]. Optimization of the current profile with external poloidal current replacement on MST has resulted in improvements in the energy confinement time approaching those values obtained in comparable low current conventional aspect ratio tokamaks while at a much lower toroidal field as shown in figure 20. The tokamak data and scaling used in figure 20 corresponds to ITER98(y,2) [62,63]. Furthermore, the central electron temperature approached 2 keV in MST. Under high current and low density conditions, reconnection events can become very large, resulting in ion temperature excursions as high as 3keV in MST. By optimizing the current profile after a reconnection event, high ion temperatures have been sustained for more than 10 ms [64].

#### 4. Confinement Experiments

The distinction between operational scenarios and confinement experiments was arguably more distinct in the past and now they increasingly overlap. More than ever, the development of operational scenarios is motivated by theoretical results and detailed diagnostic data, which were previously characteristic of focused confinement experiments. In this section, progress in understanding energy transport and turbulence, particle transport, rotation and momentum transport, L to H transition and pedestal behavior will be highlighted with emphasis given to recent diagnostic developments and measurements. A summary of theoretical developments, which are an important element of progress in this area, is given by Garbet [65].

##### 4.1 Energy transport and turbulence

The level of sophistication in testing the predictions of turbulence codes has improved by the development of increasingly comprehensive diagnostics and application of synthetic diagnostics to allow better comparisons between predictions and experimental results. A very good example of this is shown in figure 21, where the predicted density fluctuation magnitude, temperature fluctuation magnitude and the cross-phase between the electron density and temperature fluctuations are compared with the GYRO gyrokinetic calculations in L-mode discharges. As an additional and very valuable test, discharges with neutral beam heating were compared with those with combined neutral beam and electron cyclotron heating enabling the ratio of  $T_e/T_i$  to be varied. As the electron temperature was increased by electron cyclotron heating, GYRO reproduced the changes in electron density fluctuations and cross-phase in the core ( $0.4 < \rho < 0.75$ ) but over predicted the increase in temperature fluctuations that were observed. Though GYRO reproduced many of the features in the core, significant differences between the predicted and experimental heat flux exist in the edge ( $\rho > 0.75$ ) of these L-mode discharges [66]. Additional studies of DIII-D H-mode discharges were reported by [67].

Doppler reflectometry has proven to be a versatile and extensively used diagnostic to study plasma fluctuations as indicated by the many results that were presented at this meeting and it

was used to measure the turbulence spectrum in the edge of Tore Supra [68]. At smaller wavenumbers,  $k\rho_s < 0.7$ , the instabilities deposit energy into the turbulent spectrum, where the spectrum changes weakly with wavenumber and then decreases with wavenumber relatively rapidly at higher wavenumbers. A comparison was made of two discharges with different collisionalities. At  $k\rho_s \sim 0.7$  the turbulence level is higher in the higher collisionality discharge and fluctuation spectrum decreases with wavenumber at low collisionality in the low wavenumber regime. At large wavenumbers, the fit to the spectrum does not change with collisionality. Those observations are in contrast with usual expectations of the effect of collisionality on TEM or/and on zonal flows. Considering the impact of zonal flows, it is expected that a decrease of collisionality would reduce the damping on zonal flows, which would lead to a decrease of energy content on small wavenumbers due to the shearing by large scale structures. This would give a flatter wavenumber spectrum when decreasing collisionality. Alternatively, TEM instabilities would have a lower growth rate at high collisionality resulting in reduced fluctuations at short wavelengths, since only the ITB instabilities would remain. In both cases, the expectation is that the fluctuation spectrum should become peaked with  $k\rho_s$  but instead is observed to broaden at higher collisionality.

As discussed both by Razumova in her introductory talk [69] and Inagaki et al [70], nonlocal dynamics have been previously inferred in tokamaks and stellarators. Macro-scale fluctuations with long distance correlation and avalanche phenomena are possible candidates to explain the nonlocal nature role in transport [70]. On LHD, low frequency electron temperature fluctuations were measured with a multi-channel electron cyclotron emission radiometer. These measurements reveal macro-scale fluctuations, as shown in figure 22, indicating a radial correlation length that is comparable to the plasma radius. Furthermore, the fluctuations propagate radially at a ballistic speed of 1-5 km/s, approximately 50-100 times faster than what would be expected from diffusive transport in LHD. Simple estimates indicate that the effect of these instabilities is to contribute only a small portion ( $\sim 10\%$ ) of the heat flux in stationary discharges but may play an important role in transient phenomena such as cold pulse propagation. Additional evidence for nonlocal phenomenon on LHD can be found in [71]. Measurements on tokamak experiments will be interesting to determine if these low frequency fluctuations are also responsible for cold pulse propagation in tokamaks.

## 4.2 Particle and impurity transport

Particle transport with resulting changes in the density profile affects the fusion reactivity, bootstrap current profile and plasma stability and has been increasingly the focus of detailed studies. Two examples discussed above are the density profile peaking in FTU [56] and the comparison of reversed shear discharges in JET and JT-60U [47]. While for typical conditions on AUG the application of ECH leads to a flattening of the density profile, in lower current experiments the central density increases with the application of electron cyclotron heating to neutral beam heated plasmas and the ion and rotation profiles flatten. In these discharges, the measured and predicted value of  $R/L_{ne}$  increases as the ratio of  $T_e/T_i$  increases as shown in figure 23. In this comparison, the measured profiles are used as input to the quasi-linear gyrokinetic code, GS2, and the non-linear code, GYRO and the trends are shown [72].

A common (but not ubiquitous) experimental observation is that the application of perturbed magnetic fields in the edge of a tokamak results in increased particle transport and a reduction in edge density. This appears to be one of the key elements associated with ELM suppression in the DIII-D tokamak using resonant magnetic field perturbations (RMP). The decrease in density occurs over a broad range in  $q$  compared with the window for ELM suppression and the magnitude of the density decrease in the pedestal increases with coil current. (A discussion of the current understanding of ELM suppression mechanisms using RMP coils is deferred to the other summary paper [73].) The cause for the underlying increased particle transport has been studied using beam emission spectroscopy diagnostics to measure the density fluctuations on DIII-D. The magnitude of the density fluctuations increases rapidly near the top of the pedestal (few ms) with the application of the perturbed field and more slowly in the core of the plasma (20-40 ms) as shown in figure 24. The change in the fluctuation level in the core has not been correlated with local changes in the density gradients [74]. Related experiments on TEXTOR have shown that long-range correlations, associated with zonal flows, are decreased with the application of magnetic perturbations using the Dynamic Ergodic Divertor [75]. More detailed measurements in the pedestal will be valuable to determine how magnetic perturbations affect turbulence and transport and how the resulting profiles affect ELM stability.

Experiments on LHD with large ion temperature gradients observed the formation of “impurity” holes, discharges with hollow impurity profiles, as shown in figure 25. The depression in impurity concentration in the core increases with charge number. Transport analysis indicates the presence of a large outward impurity flow velocity and small diffusive coefficients as shown in figure 26. Though neoclassical transport would appear to be a possible explanation for the outward flow velocity, comparison with GSRAKE code indicates that the impurity transport should be inward due to the negative radial electric field in the core [76]. In principle, this is an ideal situation with low impurity concentration in the core and high in the edge to radiate the power; however, further understanding of the transport mechanisms is required.

Detailed studies of the evolution of impurities in the pedestal region between ELMs were performed on AUG. It was observed that after the ELM crash the impurity transport coefficients reduce to neoclassical values. In particular, the ratio of  $v/D$  increases with the charge of the impurity ions ( $\text{He}^{2+}$ ,  $\text{C}^{6+}$ ,  $\text{Ne}^{10+}$ ,  $\text{Ar}^{16}$ ) consistent with neoclassical predictions [77].

Experiments varying the plasma current and ECH power on TCV showed how the carbon density profile is affected by sawtooth activity. In low  $q$  discharges, the impurity profile can be peaked; however the carbon profile is flattened within the sawtooth mixing radius [78].

#### 4.3 Plasma rotation and momentum transport

During the past several years, experimental evidence has accumulated about the existence of intrinsic rotation in tokamaks, which has been characterized by an empirical scaling relationship based on inter-machine comparisons [79]. The first author of this publication, J. Rice, [79] accepted the Nuclear Fusion Award in 2010 at this meeting. The observations of intrinsic rotation have motivated additional, more detailed momentum transport experiments that have identified the presence of several important effects in understanding the transport of momentum in tokamak plasmas. This can be illustrated by examining the angular momentum conservation equation given below.

$$\underbrace{mR \frac{\partial nV_\phi}{\partial t}}_{\text{Rate of change of angular momentum}} = \underbrace{\sum \eta}_{\text{Input torque}} - \nabla \cdot \left( -mnR \left( \underbrace{\chi_\phi \frac{\partial V_\phi}{\partial r}}_{\text{diffusion}} - \underbrace{V_\phi V_{pinch}}_{\text{pinch}} \right) + \underbrace{\Pi_{RS}}_{\substack{\text{Residual stress} \\ \text{"Intrinsic source"}}} \right) - \underbrace{\frac{mnR(V_\phi - V_\phi^*)}{\tau_{damp}}}_{\text{Neoclassical viscous drag}} + \underbrace{\langle \tilde{J} \times \tilde{B} \rangle}_{\text{Maxwell stress}} + \dots$$

The input torque from external sources is for example calculated from the deposition of neutral beam torque. Three turbulent processes are considered: diffusion, pinch and residual stress. In addition, neoclassical viscous drag can be significant in experiments with magnetic field perturbations and fluctuating currents and magnetic fields can also exert a Maxwell stress torque. Experiments studying all of these effects have been reported and show the difficulty of simple experimental extrapolations of rotation predictions to ITER.

The Prandtl number,  $\chi_\phi/\chi_i$ , is observed to be independent of  $R/L_n$  on JET where the values and scaling are in reasonable accord within a factor of 1.5 to 2 with GS2 calculations as shown in figure 27. In contrast, the pinch parameter,  $RV_{pinch}/\chi_\phi$ , increases with  $R/L_n$  on JET also in accord with GS2 calculations as shown in figure 28. In addition consistent with experiments, the predicted pinch and Prandtl numbers do not have a strong collisionality dependence [80]. These results are generally consistent with previously reported observations of the Prandtl number and the pinch; however, the JET experimental results for the intrinsic rotation in ICRF heated discharges result in a value much lower than predicted by the empirical scaling [79,80]. For comparison, the value of the measured Prandtl number in the LHD stellarator is 0.5-1.0 [81].

These results motivate developing an understanding of the source of the intrinsic torque responsible for the intrinsic rotation in order to go beyond simple empirical scaling relationships [79]. Measurements at the edge of DIII-D H-mode plasmas find that the edge intrinsic torque, defined as the volume integral of the intrinsic torque density from  $0.8 < \rho < 1.0$ , is proportional to the edge pressure gradient as shown in figure 29. The data was obtained by sweeping the neutral beam torque in DIII-D H-mode plasmas to find conditions whereby the plasma rotation is effectively zeroed out across the profile. Under these conditions, the intrinsic torque is approximately the negative of the externally applied neutral beam torque [82]. As noted earlier, the I-mode on C-Mod has an edge temperature pedestal but not a density pedestal unlike the H-mode, which has both. A comparison of H and I-mode discharges was used to establish that the change in rotation velocity is better correlated with the change in the edge temperature gradient as shown in figure 30. While the change in core rotation,  $V_{rot}$ , is better correlated with the change in the pedestal temperature gradient, the change in angular momentum (proportional to  $nV_{rot}$ ) is better correlated with the pedestal pressure gradient and not the temperature gradient [83].

These results suggest that turbulent residual stress may be key in generating intrinsic rotation [81-84]. As discussed in [83] in the framework of residual stress, the generation process of flows can be understood as a conversion of thermal energy, which is injected into a system by heating, into macroscopic flow by drift wave turbulence excited by  $\nabla T$ ,  $\nabla n$ , etc. In the linear device, CSDX, the Reynold's stress have been observed to be sufficient to account for the intrinsic rotation [83]; however, in experiments on DIII-D, probe measurements in low power neutral beam heated discharges indicate that the Reynold's stress at the boundary is approximately zero

and additional mechanisms are needed to understand the intrinsic rotation [82].

In addition to the intrinsic torque in the edge region from temperature and pressure gradients, intrinsic core torques in the core, which are typically small compared with the edge torque, can affect the rotation profile. Analysis of the rotation profile in JT-60U H-mode discharges with strong pressure gradients indicates that better agreement is obtained by including a residual stress proportional to the ion pressure gradient,  $\Pi_{\text{res}} = \alpha_{k1} \chi_{\phi} \nabla P_i$  where the constant  $\alpha_{k1}$  is assumed to be independent of minor radius, as shown in figure 31 [84]. Analysis of the intrinsic torque in a DIII-D H-mode discharge, shown in figure 32, indicates the presence of torque in the counter direction in the core and a large positive torque in the edge. In addition, measurements on DIII-D indicate that ECH can generate counter torque in the core [82]. Also on LHD, the existence of temperature gradient effects on the momentum transport in the core was also observed in ion ITB plasmas [81].

Magnetic field perturbations due to low-n coils as well as more localized perturbations including toroidal field ripple have been studied on a number of devices, [42, 51, 60, 80, 85, 86]. Experiments on Tore Supra indicate that as the toroidal ripple is increased, the plasma rotates in the counter-direction, as expected from neoclassical predictions taking into account ripple-induced thermal toroidal friction, though the poloidal flow dynamics are not yet understood [85]. Tests on DIII-D, simulating the ferromagnetic field error from the ITER Test Blanket Modules, showed that the plasma rotation decreased as much as 50% over the entire radial profile due to non-resonant braking [42]. Neoclassical toroidal viscosity (NTV) braking by the mock-up field was evaluated using IPEC, which was found to overestimate the measured torque by a factor of 3. The authors considered this to be in fair agreement considering the simplifying assumptions employed [87]. As noted in [51], previous non-resonant magnetic field perturbation experiments on DIII-D have shown that the effect of NTV is to accelerate a co-rotating plasma towards the neoclassically predicted offset velocity in the counter direction, a key prediction. While a more quantitative agreement between theory and experiment, which includes the plasma response to the applied magnetic perturbations, is needed, many of the predictions regarding NTV are coming into focus and already are being used to guide experiments.

MHD instabilities in the core can also modify the rotation profile. Charge exchange recombination measurements together with conditional averaging have been used on TCV to evaluate the effect of the sawtooth crash on the rotation profile in ECH heated discharges. In the core region, initial results indicate a fast (<2 ms) co-current acceleration following a sawtooth crash and a counter-current acceleration outside of the inversion radius, as shown in figure 33. The rotation profile relaxes on a time scale of ~5 ms until the process repeats itself. The authors suggest that the sawtooth crash may be responsible for the empirical rotation scaling relationship [88].

Detailed measurements of the Maxwell stress induced change in the plasma flow, approximately given by,

$$\int T_{//,i} \nabla \frac{\langle \delta n \delta b_r \rangle}{B} dt$$

were performed on the reversed field pinch, MST, following a sawtooth event. The fluctuating

density and magnetic field as well as the ion temperature, which is approximately constant with minor radius, were measured along with the parallel velocity. The change in the flux induced flow is in good agreement with the observed change in the measured flow, as shown in Fig. 34. The authors conclude that these MHD events, associated with nonlinear mode-mode coupling are an important element in generating a significant momentum flux in MST [89].

The combination of high quality profile data, flexible heating systems that can vary the applied torque and development of new analysis techniques have been instrumental in revealing many new phenomena. This increased understanding may provide opportunities to tailor the rotation profile, which can affect transport and stability. An example of this is the new work on the QH mode using magnetic perturbations [51]. Nonetheless, in the short term, the complexity of the phenomena presents a challenge to predict the rotation profile in ITER, which has a direct consequence on the predictions of particle and thermal transport.

#### 4.4 L to H-mode transition

Understanding the physics responsible for the L to H transition is both important for extrapolating to ITER as discussed in Sec. 3.5 and is a very complex and interesting physics topic in itself. The application of new diagnostics and the study of the transition in both tokamaks and stellarators have provided new insights into this problem. A key diagnostic in many of the experiments was Doppler reflectometry, which enables not only the measurement of density fluctuations but also measurements of oscillating radial flows. Furthermore, this diagnostic can be used in higher power discharges, which are not compatible with extensive probe measurements.

An outstanding issue in understanding the transition from L to H-mode is the relative roles of the mean shear in the radial electric field and the fluctuating sheared flows. Experiments on MAST [41], NSTX [39] and TJ-II [90-92] have reported no significant change in mean shear in the radial electric field immediately prior to the transition. As shown in figure 35 from results on TJ-II [90, 91], there is an abrupt change in the density fluctuation magnitude at the time of the L to H transition time while the shear in the mean radial electric field decreases afterwards. This is an example of an abrupt transition. In some conditions, gradual transitions from L to H-mode have been studied to understand the interplay between the fluctuation level and the electric field. Close to the L-H transition threshold, pronounced oscillations in both,  $E_r$  and density fluctuation level, are measured within the radial range  $\rho \approx 0.75 - 0.83$  that are not detected at  $\rho > 0.83$ .

Analysis of the signals reveals an increase in the fluctuations of the radial electric field,  $E_r$ , and  $E_r$  field shear within the frequency range 1–10 kHz just at the transition. The increase in the low frequency  $E_r$  fluctuations and the reduction in the high frequency density fluctuations are measured a few ms before the  $E_r$  field shear development [91]. Analysis of the Doppler reflectometer signals in discharges with a slow L to H transition enables the study of the coupling between the sheared flows and turbulence. The color contour map in figure 36 shows the magnitude of the density fluctuations while the frequency is related to  $E_r$ . The temporal relationship between the oscillating  $E_r$  and the density fluctuations are shown in figure 37 for the data shown in figure 36. The time evolution of both,  $E_r$  and density fluctuations, indicates a characteristic predator-prey relationship: a periodic behavior with  $E$  (predator) following the

density fluctuation level (prey) with a  $90^\circ$  phase difference as shown in Fig. 38. The turbulence induced flow shear is generated causing a reduction in the density fluctuations and a subsequent drop in the flow shear, which is followed by the increase in the density fluctuations [90-92]. These results have many of the characteristics of the predicted dynamics of L to H transition models based on turbulence driven flows. One empirical question is whether this is a high frequency dithering H-mode, with many back and forth transitions between L and H-mode or the underlying trigger mechanism for the H-mode.

Complementary experiments on AUG were performed also using Doppler reflectometry in low density and high electron temperature discharges. This is a regime in which the transition from L to H-mode goes through an intermediate state (called the I-phase). This intermediate phase can last for many seconds and is characterized by weak H-mode energy confinement but without a temperature pedestal and no ELMs. In this state, large GAMs are more clearly observed. Above a turbulence threshold on a sub- $\mu$ s timescale, the radial electric field oscillations, which are identified to be GAMs with a frequency  $\sim 16$ kHz, grow, reducing the amplitude of the turbulence and then are suppressed. The cycle then begins again, with the turbulence growing, leading to another burst of radial electric field oscillations. This appears to be classic limit-cycle behavior. These instabilities are located in the edge region and the spatial extent and location of the GAMs changes with the minimum of the mean electric field shear indicating a linkage between the mean and oscillating fields. At higher power, the pulsing is observed to diminish, the  $D_\alpha$  emission drops and a transition to a weak ELM-free H-mode is observed and the coherent GAM oscillation is replaced by large amplitude broad-band flow fluctuations [93]. These results are suggestive that GAMs are a missing link during the intermediate phase prior to the transition to H-mode. An intriguing question related to operational scenarios is what is the relationship the AUG I(ntermediate)-phase and the C-Mod I-mode? There appear to be tantalizing similarities as well as differences, since in the I-mode a temperature pedestal is observed though not in the I-phase.

In addition to measurements of GAMs, further studies of zonal flows have been conducted on a number of devices. Probe measurements in the edge, near the last-closed-flux surface (LCFS) of HL-2A indicate that GAMs are dominant; however, further inside GAMs and zonal flows coexist, as shown in Fig. 39 [94]. The poloidal and toroidal mode number were measured using probes. The energy partition among the low frequency zonal flows (LFZF), the GAM and the ambient turbulence (AT), suggests that the GAM predominantly suppresses the AT near the LCFS, while both the GAM and LFZF have significant effects on the AT in the inner region of the plasma. Long-range correlations consistent with the theory of zonal flows have been studied on TJ-II, TJ-K, TEXTOR, ISTTOK, and RFX-mod, spanning stellarators, tokamaks, and reversed field pinch configurations using a combination of probes and biased limiters [75]. An extensive set of results has been obtained and only some of the highlights will be mentioned here. Low frequency long-range correlations in the zonal flows as measured by potential fluctuations are amplified during the development of edge mean electric field shear using electrode biasing in TJ-II and TJ-K stellarators and TEXTOR and ISTTOK tokamaks and during the spontaneous L to H transition in TJ-II. Evidence for non-local energy transfer has been observed in the TJ-K stellarator. The authors conclude that the results point to a significant link between ExB sheared flows, long-range correlations and transport bifurcations. Long-range correlations are strongly reduced as the density approaches the density limit in TEXTOR and TJ-

II, implying the possible role of collisionality and/or impact of mean flow shear on zonal flows [75]. An overview of stellarator H-mode experiments was presented in [95] and illustrates how stellarator experiments are complementary to tokamak experiments in probing the underlying physics and in identifying additional important issues such as the resonances in the rotational transform.

The progress in diagnosing the complex interplay between the mean flow shear, the background turbulence and the zonal flows and GAMs prior to an L to H transition has been substantial. Further work to conclusively understand the complex dynamics may require additional measurements of the spatial evolution of the turbulent structure. At present despite substantial experimental progress, a predictive capability for the L to H transition based on plasma turbulence does not exist and reliance on scaling relationships continues.

#### 4.5 Pedestal

The pressure at the top of the pedestal in H-mode discharges strongly impacts global confinement and is predicted to affect fusion performance in ITER. Furthermore, a large pressure gradient can result in destabilization of ELMs by the peeling-ballooning mode. Extensive comparisons between profile measurements prior to an ELM crash and the predictions of stability of the peeling-ballooning mode have been performed and are in generally good agreement [96]. The height and width of the pedestal is a complex interplay of turbulent processes and macro-stability determining the onset of ELMs. New more accurate diagnostics with better time resolution are enabling more detailed tests of the underlying assumptions used to model the dynamics of the pedestal.

Detailed measurements of the evolution of the temperature and density gradients during the recovery phase after an ELM crash on AUG show that the pressure gradients saturate approximately half way through the ELM cycle with differences observed in how the electron density and temperature evolves. Since no direct measurements of the current profile are available on AUG, the edge current density was evaluated. The predicted bootstrap current drops rapidly after the ELM crash as would be expected and quickly is restored when the temperature and density gradients saturate. The total current density according to this analysis is restored within 1ms of the bootstrap current. Hence the delay to the onset of the next ELM is not yet explained [77]. Whether the delay is associated with more subtle effects such as the dependence on gradients near the top of the pedestal, since the peeling-ballooning modes are global and not local, remains to be determined.

A new Motional Stark Effect diagnostic has been made operational on MAST to measure the edge toroidal current density [41]. These measurements have been compared with neoclassical calculations of the bootstrap current as shown in figure 40. After the ELM crash, there is a major difference between the measurements and the bootstrap calculations. Since this comparison assumes that the current profile is in equilibrium that might not be a good assumption after the ELM crash. Late in time, the peak of the bootstrap current calculations are in approximate agreement with experiments though the measured current profile is broader. If this were due to spatial resolution of the measurements then the peak of the measured profile would exceed the predictions. Another new diagnostic, based on electron Bernstein wave emission possessing

higher spatial resolution than MSE, indicates that the MSE measurements of the total edge current are correct but that the current profile is more peaked, in disagreement with the bootstrap current predictions. Using the measured toroidal current profile from MSE and electron pressure profile on MAST, it is inferred that the plasmas linger for 10-20 ms at or above the predicted peeling-ballooning stability boundary. Whether this is because the theory is incomplete or a result of the uncertainties in the edge profile measurements is a topic of future work [41]. Nonetheless, these new measurements, when coupled to more detailed analysis, will provide an important tool to analyze the stability in the edge.

Further extension of the EPED model to version EPED1.6 showed good agreement with experimental data from C-Mod, DIII-D and JET [96]. The EPED model combines peeling-ballooning and kinetic ballooning mode (KBM) physics to predict pedestal height and width. The KBM is a pressure gradient driven mode, with an abrupt linear onset resulting in large transport. In QH experiments on DIII-D with large toroidal rotation, high frequency coherent modes ( $\sim 80\text{-}220$  kHz) with a dominant toroidal mode number  $n\sim 19$  and poloidal mode numbers  $m\sim 55\text{-}104$  are observed. The mode frequency in the plasma frame is found to be close to 0.2–0.3 times the local ion-diamagnetic frequency. These modes exhibit a number of features that are qualitatively similar to characteristics predicted for KBM:  $n$ -number, poloidal mode structure, frequency separation and mode velocity, though mode identification will require more detailed modeling [74]. Extending these fluctuation studies to ELMy H-mode discharges will enable further direct tests of the EPED model.

#### 4.6 Confinement implications of ELM mitigation

As noted earlier, the control of ELMs was a major topic at this topic and will be addressed further in the summary paper by Jacquinot [73]. ELM mitigation has been explored on a number of machines using different approaches. One of the important aspects in evaluating different ELM mitigation techniques, in addition to whether they will sufficiently reduce the transient heat load from ELMs and the engineering implications, is the impact on plasma density and confinement since ITER is projected to operate near the Greenwald limit and requires H-factors of one to achieve  $Q_{DT} = 10$ .

Results from JET have compared different ELM mitigation techniques as shown in figure 41. The application of plasma kicks (sudden vertical movement of the plasma) or magnetic perturbations using the error field correction coils (EFCC) result in a decrease in plasma density. Gas puffing can compensate the density decrease; however, a significant reduction in confinement time then is observed. The more direct comparison of the effect on the plasma stored energy in discharges, where kicks were used to stimulate ELMs, is shown in figure 42. Due to the density dependence in H-mode confinement scaling for  $H_{98(y,2)}$ , the H-factor stays relatively constant though the stored energy declines. The reduction in stored energy appears to saturate with increased ELM frequency, which is encouraging, since in ITER it may be necessary to increase the frequency by a factor of  $\sim 20$  [29,50]. An implication of these experiments is that in ITER it is probable that in order to avoid damage to divertor target plates by ELMs some reduction in the maximum fusion performance will be necessary. Since  $Q_{DT}$  is a sensitive function of confinement time and large reductions in the energy deposition relative to that from

unmitigated ELMs are necessary, further research is needed to determine how to make this tradeoff.

## **5. Conclusions**

Substantial progress in the development of operational scenarios and understanding the underlying transport mechanisms were reported on at this meeting. Increasingly sophisticated diagnostics are being coupled with cutting edge theoretical and computational models to improve our understanding and to guide the development of operational scenarios. These are significant contributions to future successful operations on ITER [16] and W7-X [17], which are under construction.

The cross-fertilization between tokamak, stellarator and reverse field pinch configurations has yielded new insights and been valuable in enhancing the research on all configurations. This is reflected in many ways ranging from detailed experiments to understand the underlying transport mechanisms such as the L to H transition to adopting operational techniques such as lithium coatings and using common diagnostic developments such as Doppler reflectometry.

Innovative confinement concepts enable scientific exploration of interesting physics issues and may provide alternative approaches to aid in the development of fusion.

Acknowledgments: This paper is the result of the hard work of the authors at the IAEA meeting and I want to express my appreciation for permission to use their figures and many interesting discussions. The author of this report has also benefitted from the input of his colleagues, E. Belova, D. Gates, T. S. Hahm, S. Kaye, C. Kessel, R. Maingi, G. H. Neilson, S. Prager, T. Simonen, W. Solomon, J. R. Wilson and M. Zarnstorff who amidst a very busy conference provided valuable perspectives. Of course, the author is responsible for errors in describing the results of this meeting. The work was supported in part by U.S. DOE Contract DE-AC02-76CH03073.

## References

References presented below as papers at this conference are available online at [http://www-pub.iaea.org/mtcd/meetings/cn180\\_papers.asp](http://www-pub.iaea.org/mtcd/meetings/cn180_papers.asp)

- [1] Garnier, D. T. *et al* Turbulent Particle Pinch in Levitated Superconducting Dipole ICC/1-1Ra
- [2] Saitoh, H. *et al* High-Beta Plasma Confinement and Inward Particle Diffusion in the Magnetospheric Device RT-1 EXC/9-4Rb
- [3] Belova, E. V. *et al* Two-Fluid Mechanism of Plasma Rotation in Field-Reversed Configuration ICC/P5-02
- [4] Inomoto, M. *et al* Kinetic Behaviors of Energetic Ions in Oblate Field-Reversed Configuration ICC/P7-01
- [5] Kruglyakov, E.P. *et al* Progress in studies of magnetic mirror and their prospects. OV/P-6
- [6] Burdakov, A.V. *et al* New Experiments on the GOL-3 Multiple Mirror Trap EXC/P4-03
- [7] Bagryansky, P.A. *et al* Vortex confinement of hot ion plasma with  $\beta=0.6$  in axially symmetric magnetic mirror EXC/P8-02
- [8] Yoshikawa, M. *et al* Fluctuation Suppression during the ECH induced Potential Formation in the Tandem Mirror GAMMA 10 EXC/P8-21
- [9] Asai, T. *et al* Active Stability Control of a High-Beta Self-Organized Compact Torus ICC/P5-01
- [10] Oishi, T. *et al* Helical-Tokamak Hybridization Concepts for Compact Configuration Exploration and MHD Stabilization ICC/P5-04
- [11] Ryzhkov, S. V. *et al* Modeling of High Density and Strong Magnetic Field Generation by Plasma Jet Compression ICC/P5-05
- [12] Nagata, M. *et al* Demonstration of Multipulsed Current Drive Scenario using Coaxial Helicity Injection in the HIST Spherical Torus Plasmas EXC/P2-04
- [13] Jarboe, T.R. *et al* Recent results from the HIT-SI experiment ICC/P5-03
- [14] Takeno, H. *et al* Improvement of Cusp Type and Traveling Wave Type Plasma Direct Energy Converters Applicable to Advanced Fusion Reactor ICC/P7-02
- [15] Stork, D. *et al* The upgrade to the Mega Amp Spherical Tokamak ICC/P5-06
- [16] Motojima, O. Progress in ITER Construction OV/2-2
- [17] Bosch, H.S. *et al* Overview of the construction and scientific objectives of the Wendelstein 7-X stellarator EXC/2-5Rb
- [18] Morisaki, T. *et al* Progress of Superdense Plasma Research in LHD: Sustainment and Transport Study EXC/1-5
- [19] Takahashi, H. *et al* High Te, low collisional plasma confinement characteristics in LHD EXC/P8-15
- [20] ITER Physics Basis Editors *et al* 1999 *Nucl. Fusion* **39**
- [21] Shimada, M. *et al* 2007 'Progress in the ITER Physics Basis' *et al* 2007 *Nucl. Fusion* **47** S1
- [22] Kwon, M. *et al* Overview of KSTAR Initial Experiments OV/1-1
- [23] Wan, B.N. *et al* Recent Progress in High Power Heating and Long Pulse Experiments on EAST OV/1-2

- [24] Douai, C. *et al* Recent Results on ICRF Assisted Wall Conditioning in Mid and Large Size Tokamaks FTP/P1-26
- [25] Jackson, G. L. *et al* DIII-D Experimental Simulation of ITER Scenario Access and Termination EXS/P2-11
- [26] Tuccillo, A. A. *et al* Overview of the FTU Results OV/4-4
- [27] Marmar, E. S. *et al* Overview of Recent Results from Alcator C-Mod including Applications to ITER Scenarios OV/3-2
- [28] Ferreira Nunes, I.M. *et al* Confinement and Edge studies towards low  $\rho^*$  and  $\nu^*$  at JET EXC/P8-03
- [29] De la Luna, E. *et al* Effect of ELM mitigation on confinement and divertor heat loads on JET EXC/8-4
- [30] Romanelli, F. *et al* Overview of JET Results OV/1-3
- [31] Sips, A.C.C. *et al* ITER ramp-up and ramp-down scenarios studies in helium and deuterium plasmas in JET EXC/P2-08
- [32] Wilson, J.R. *et al* Experiments and Simulations of ITER-like Plasmas in Alcator C-Mod EXC/P2-02
- [33] Schweinzer, J. *et al* Confinement of ‘Improved H-modes’ in the All-Tungsten ASDEX Upgrade EXC/P2-07
- [34] Hughes, J.W. *et al* Power requirements for superior H-mode confinement on Alcator C-Mod: Experiments in support of ITER EXC/P3-06
- [35] Giroud, C. *et al* Integration of a radiative divertor for heat load control into JET operational scenarios EXC/P3-02
- [36] Martin, Y. R. *et al* 2008 *Journal of Physics: Conference Series* **123** 012033
- [37] Gohil, P. *et al* L-H Transition Studies on DIII-D to Determine H-mode Access for Non-Nuclear Operational Scenarios in ITER EXC/2-4Ra
- [38] Mc Donald, D.C. *et al* JET Helium-4 ELMy H-mode studies EXC/2-4Rb
- [39] Kaye, S.M. *et al* L-H Threshold Studies in NSTX EXC/2-3Rb
- [40] Ryter, F. *et al* 2009 *Nucl. Fusion* **49** 062003
- [41] Meyer, H. *et al* L/H transition and pedestal studies on MAST EXC/2-3Ra
- [42] Schaffer, M. J. *et al* ITER Test Blanket Module Error Field Simulation Experiments at DIII-D ITR/1-3
- [43] Joffrin, E. H. *et al* High confinement hybrid scenario in JET and its significance for ITER EXC/1-1
- [44] Luce, T.C. *et al* Development of Advanced Inductive Scenarios for ITER ITR/1-5
- [45] Politzer, P.A. *et al* Understanding Confinement in Advanced Inductive Scenario Plasmas — Dependence on Gyroradius and Rotation EXC/P2-06
- [46] Mantica, P. *et al* A Key to Improved Ion Core Confinement in JET Tokamak: Ion Stiffness Mitigation due to Combined Plasma Rotation and Low Magnetic Shear EXC/9-2
- [47] Litaudon, X. L. *et al* Core Transport Properties in JT-60U and JET Identity Plasmas EXC/P4-12
- [48] Mailloux, J. *et al* Towards a Steady-State Scenario with ITER Dimensionless Parameters in JET EXC/1-4
- [49] Ferron, J. R. *et al* Optimization of the Safety Factor Profile for High Noninductive Current Fraction Discharges in DIII-D EXS/P2-06

- [50] Loarte, A. *et al* ITER ELM control requirements, ELM control schemes and required R&D ITR/1-4
- [51] Garofalo, A.M. *et al* Advances Toward QH-mode Viability for ELM-Free Operation in ITER EXS/1-2
- [52] Whyte, D.G. *et al* I-mode: An H-mode energy confinement regime with L-mode particle confinement on Alcator C-Mod EXC/1-3
- [53] Whyte, D. G. *et al* 2010 *Nucl. Fusion* **50** 105005. doi: [10.1088/0741-3335/52/12/124048](https://doi.org/10.1088/0741-3335/52/12/124048)
- [54] Raman, R. *et al* Overview of Physics Results from NSTX OV/2-4
- [55] Maingi, R. *et al* Modification of Edge Profiles, Edge Transport, and ELM Stability with Lithium in NSTX EXD/2-2
- [56] Mazzitelli, G. *et al* FTU results with the liquid lithium limiter EXC/6-3
- [57] Martin, P. *et al* Overview of the RFX Fusion Science Program OV/5-3Ra
- [58] Sánchez, Joaquín *et al* Overview of TJ-II Experiments OV/4-4
- [59] Maingi, R. *et al* 2010 *Phys. Rev. Lett.* **105** 135004
- [60] Canik, J.M. *et al* Optimization of Density and Radiated Power Evolution Control using Magnetic ELM Pace-making in NSTX EXC/8-1
- [61] Majeski, R. *et al* First Results from the Lithium Tokamak eXperiment (LTX) ICC/P3-01
- [62] Chapman, B. E. *et al* Helical structures and improved confinement in the MST RFP EXC/P5-01
- [63] Chapman, B. E. *et al* 2010 *Plasma Phys. Control. Fusion* **52** 124048
- [64] Almagri, A.F. *et al* Non-collisional ion heating and magnetic turbulence in the RFP EXC/P8-01
- [65] Garbet, X. Summary Talk on Magnetic Confinement Theory and Modeling S/1-3
- [66] Rhodes, T.L. *et al* Multi-scale/Multi-field Turbulence Measurements to Rigorously Test Gyrokinetic Simulation Predictions on the DIII-D Tokamak EXC/7-2
- [67] Schmitz, L. *et al* Reduced Electron Thermal Transport in Low Collisionality H-mode Plasmas in DIII-D and the Importance of Small-Scale Turbulence EXC/P7-01
- [68] Vermare, L. *et al* Impact of collisionality on fluctuation characteristics of micro-turbulence EXC/P8-19
- [69] Razamuva, K. Another look at Tokamak Plasma Physics FPM/1
- [70] Inagaki, S. *et al* Radial Structure of Fluctuation in Electron ITB Plasmas of LHD EXC/7-4Ra
- [71] Tamura, N. *et al* Edge-Core Interaction Revealed with Dynamic Transport Experiment in LHD EXC/P8-16
- [72] Kallenbach, A. *et al* Overview of ASDEX Upgrade results OV/3-1
- [73] Jacquinet, J. Summary Talk on Sessions EX/S, EX/D, EX/W S/1-2
- [74] Yan, Z. *et al* Pedestal Turbulence Dynamics in ELMing and ELM-Free H-Mode Plasmas EXC/P3-05
- [75] Xu, Y. *et al* Long-Range Correlations and Edge Transport Bifurcation in Fusion Plasmas EXC/9-3
- [76] Yoshinuma, M. *et al* Impurity transport of ion ITB plasmas on LHD EXC/9-1
- [77] Kurzan, B. *et al* Transport in-between edge localized modes in the pedestal of ASDEX Upgrade EXC/P3-03
- [78] Martin, Y. *et al* Impurity Transport in TCV: Neoclassical and Turbulent Contributions EXC/P8-13

- [79] Rice, J.E. *et al* 2007 *Nucl. Fusion* **47**, 1618
- [80] Tala, T. *et al* JET Rotation Experiments towards the Capability to Predict the Toroidal Rotation Profile EXC/3-1
- [81] Nagaoka, K. *et al* Heat and Momentum Transport of Ion Internal Transport Barrier Plasmas on Large Helical Device EXC/P4-08
- [82] Solomon, W.M. *et al* Characterization of the Effective Torque Profile Associated with Driving Intrinsic Rotation on DIII-D EXC/3-5
- [83] Rice, J. E. *et al* Progress towards a physics based phenomenology of intrinsic rotation in H-mode and I-mode EXC/3-3
- [84] Yoshida, M. *et al* Core and edge toroidal rotation study in JT-60U EXC/3-2
- [85] Fenzi, C. *et al* On Plasma Rotation with Toroidal Magnetic Field Ripple and No External Momentum Input EXC/3-4
- [86] Urano, H. *et al* Comparison of pedestal characteristics in JET & JT-60U similarity experiments under variable toroidal field ripple EXC/P8-17
- [87] Park, J.K. *et al* Robust Correction of 3D Error Fields in Tokamaks including ITER EXS/P5-12
- [88] Duval, B.P. *et al* Momentum Transport In TCV Across Sawteeth Events EXS/P4-01
- [89] Brower, D.L. *et al* Fluctuation-Induced Momentum Transport and Plasma Flows in the MST Reversed Field Pinch EXC/P4-02
- [90] Estrada, T. *et al* L-H transition experiments in the TJ-II stellarator EXC/P3-01
- [91] Estrada, T. *et al* 2009 *Plasma Phys. Control. Fusion* 51 124015
- [92] Estrada, T. *et al* 2010 *EPL* **92** 35001 DOI: 10.1209/0295-5075/92/35001
- [93] Conway, G.D. *et al* Behaviour of mean and oscillating ExB plasma flows and turbulence interactions during confinement mode transitions EXC/7-1
- [94] Zhao, K. *et al* Experimental Study of Zonal Flow, Geodesic Acoustic Mode and Turbulence Regulation in Edge Plasmas of the HL-2A Tokamak EXC/7-3
- [95] Hirsch, M. *et al* H-mode in Helical Devices EXC/2-5Ra
- [96] Snyder, P.B. *et al* A First Principles Predictive Model of the Pedestal Height and Width: Development, Testing, and ITER Optimization with the EPED Model THS/1-1

## Figures

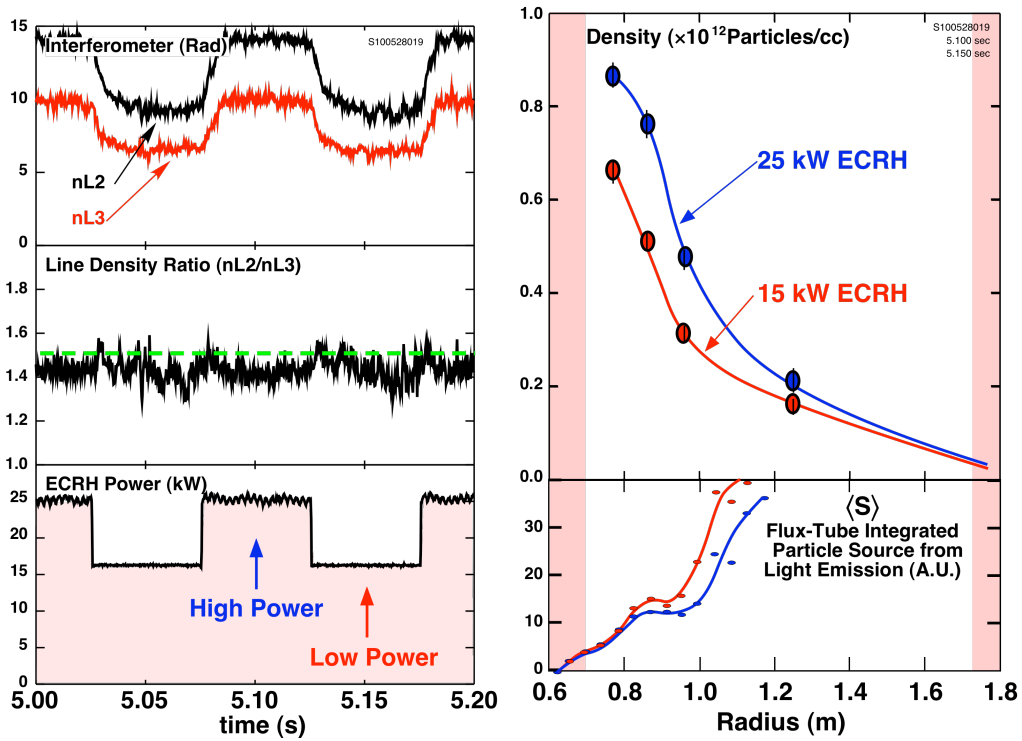


**Figure 1.** Evolution of the plasma density in LDX following strong modulation of the microwave heating power in left hand plot. The density modulates while maintaining near stationary profile shapes as indicated by the line density ratio of the interferometer in the left hand plot and the green curve is for comparison. The density profiles are shown in the right hand plot. [1].

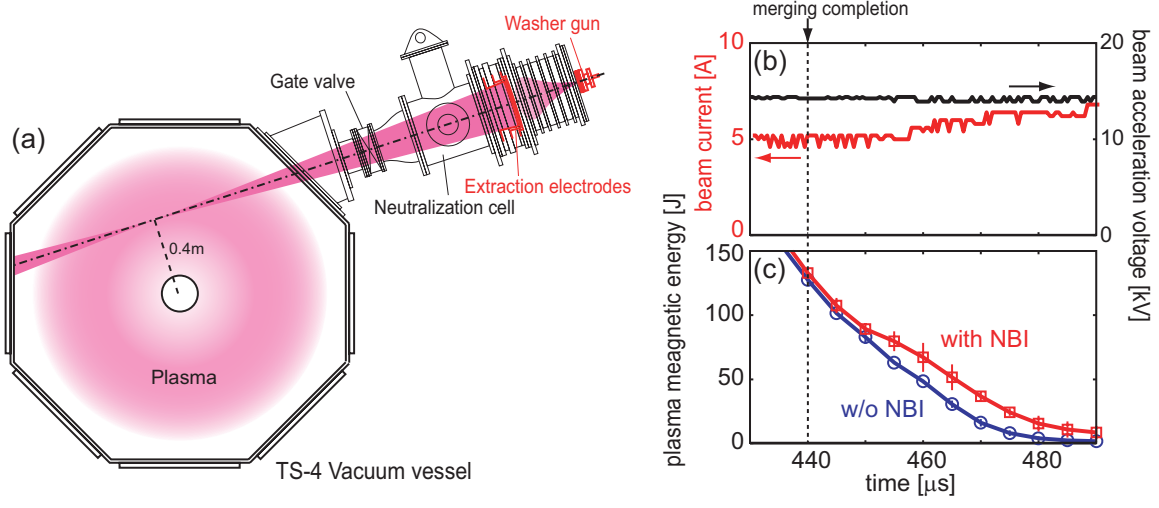


**Figure 2.** (a) Cross-sectional view of the TS-4 device with neutral beam source. (b) Time evolution of neutral beam voltage and current, (c) and FRC stored energy [4].

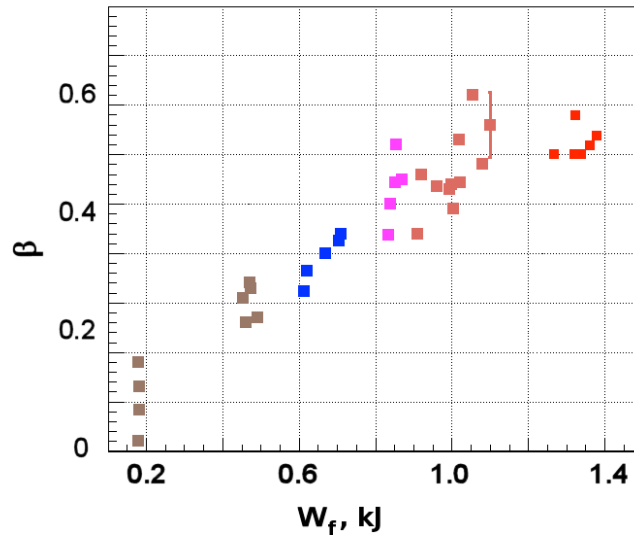


**Figure 3.** Plasma beta measured with motional Stark effect diagnostic in the fast ion turning point versus energy accumulated in fast ions in the gas dynamic trap. The brown points correspond to one and two injector; the blue points to four injectors, the magenta to five injectors, the light brown to six injectors at 2.8 kG while the red points correspond to six injectors at 3kG [5].

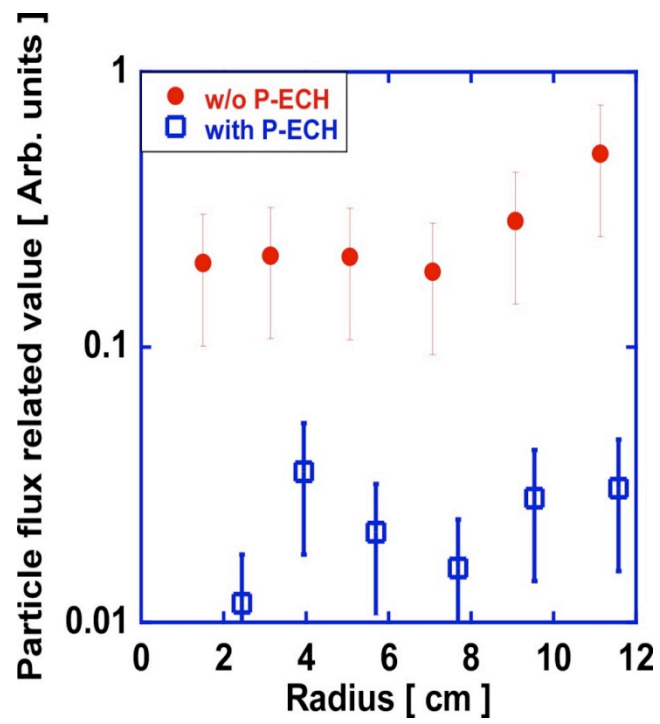


**Figure 4.** The radial particle flux related value without (closed circles) and with P-ECH (open squares) in GAMMA-10 [8].

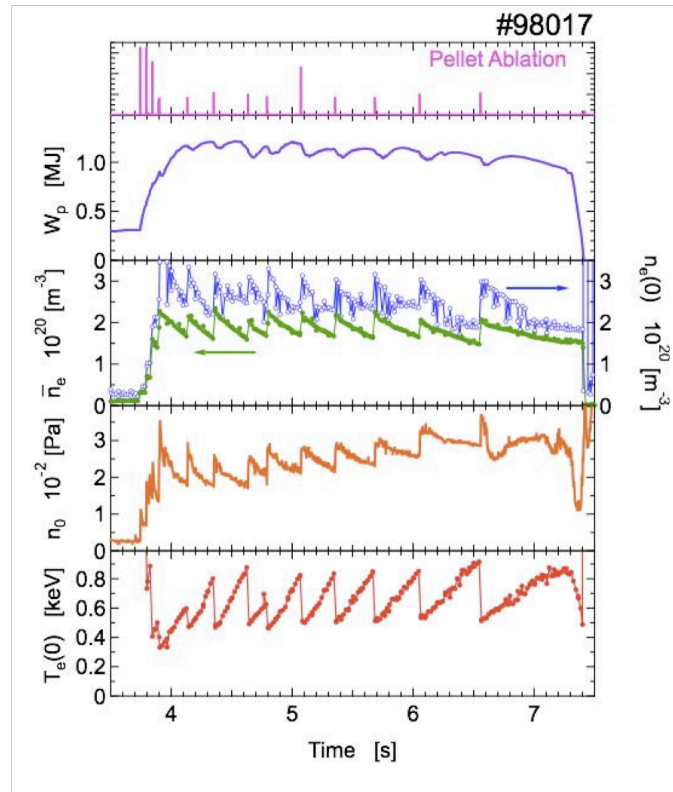


**Figure 5.** Time traces from LHD of stored energy  $W_p$ , line averaged density,  $n_e$ , central density  $n_e(0)$ , neutral pressure which is reflected with particle density  $n_0$ , and temperature  $T_e(0)$ , together with pellet ablation injection signal top [18].

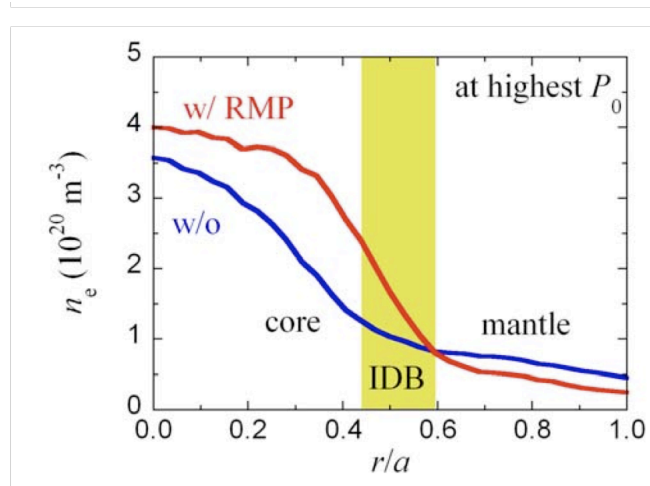


**Figure 6.** Radial electron density profiles in LHD with and without the application of RMP. Note the three regions, core, IDB and mantle [18].

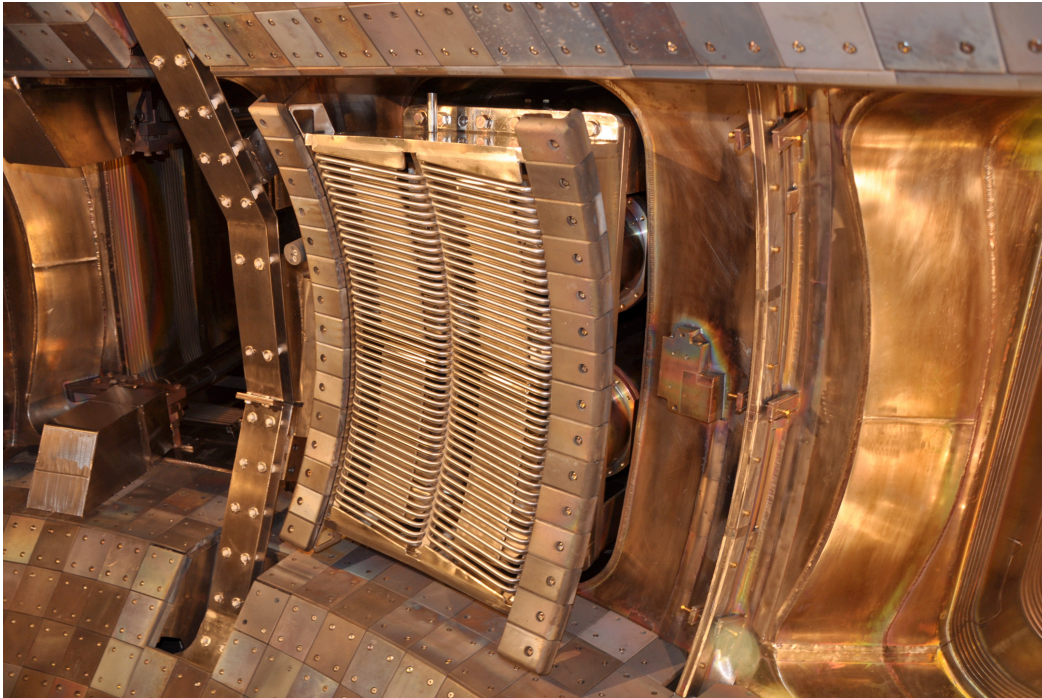


**Figure 7.** The ICRF antenna used for plasma heating is in the center of the picture and the dedicated antenna used to condition the walls in EAST is shown to the left of the antenna [23].

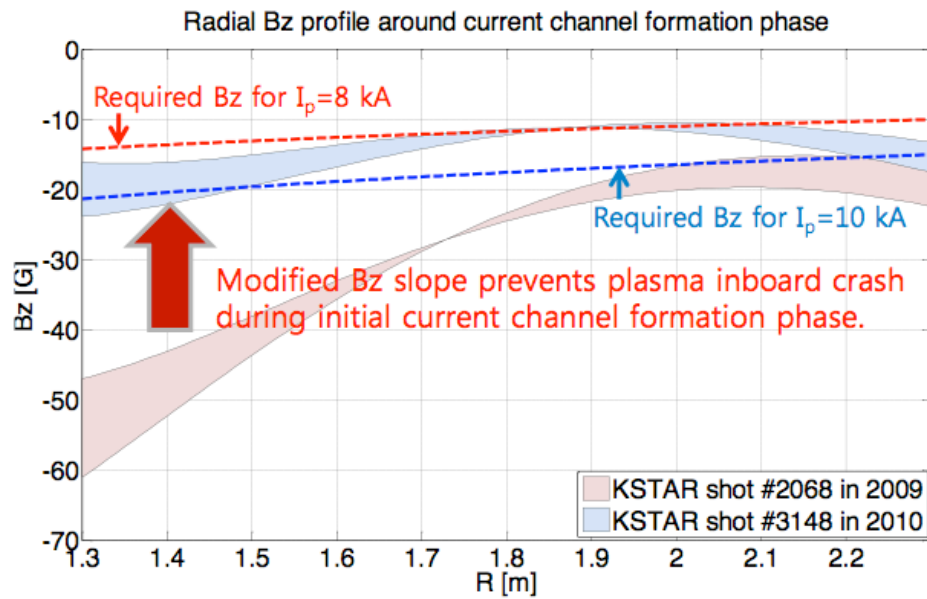


**Figure 8.** The effect of ferromagnetic Incoloy 908 alloy in the superconducting cable conduit on the vertical magnetic field in the plasma was evaluated. The vertical field was then compensated to enable the KSTAR start-up scenario [22].

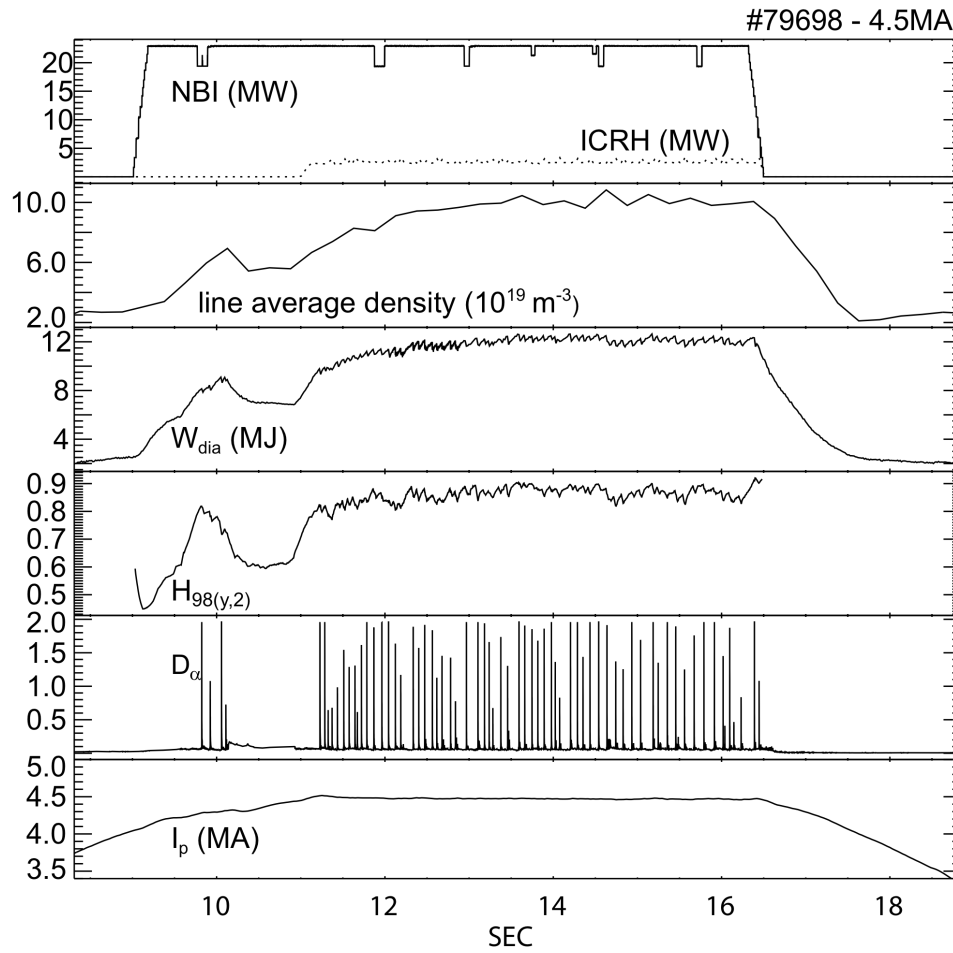


**Figure 9.** Time traces of a 4.5MA JET discharge [28].

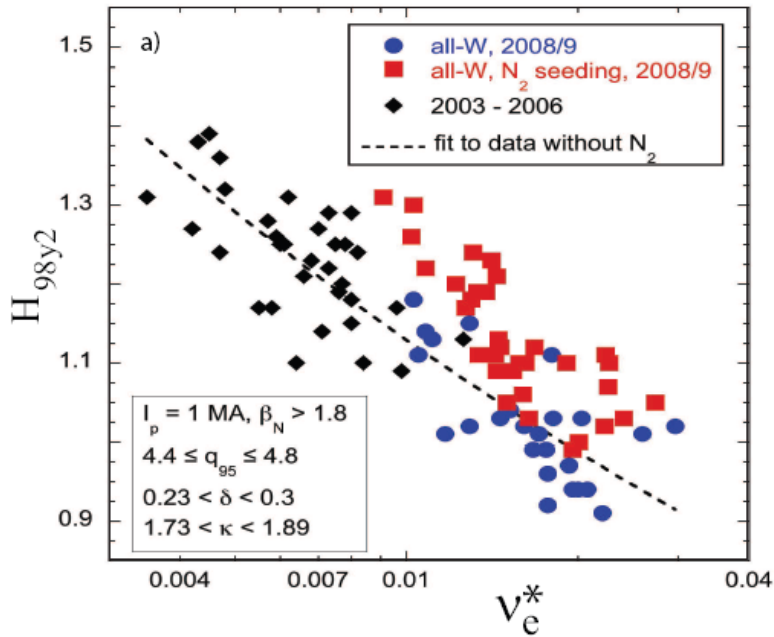


**Figure 10.** H-mode confinement enhancement factor,  $H_{98(y,2)}$ , dependence on collisionality for ‘early’ (blue and red symbols) and ‘late’ heated (black symbols) improved H-mode discharges. In 2008/9 all discharges use the early heating approach and have at least 0.8MW of ECRH power. The blue full circles refer to operation without N<sub>2</sub> seeding, while the red points are with N<sub>2</sub> seeding [33].

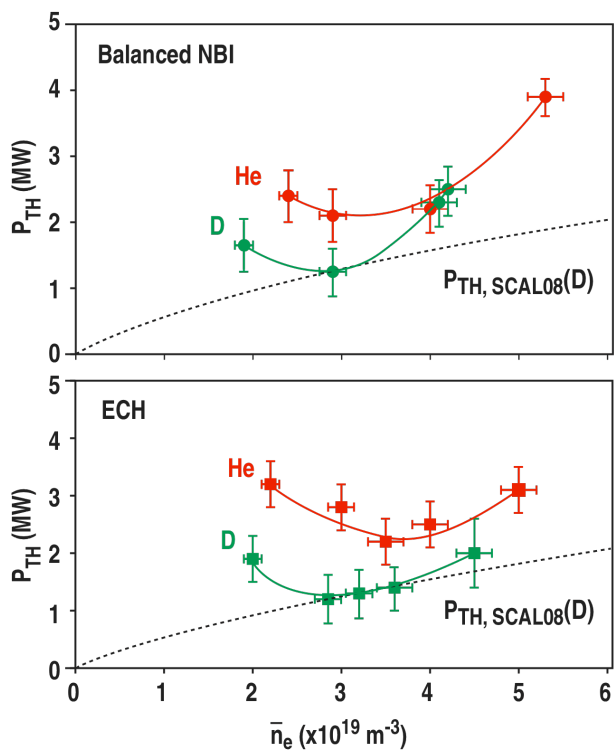


**Figure 11.** The power threshold for the L to H transition in helium and deuterium DIII-D discharges. The scaling relationship is calculated for deuterium discharges [37].

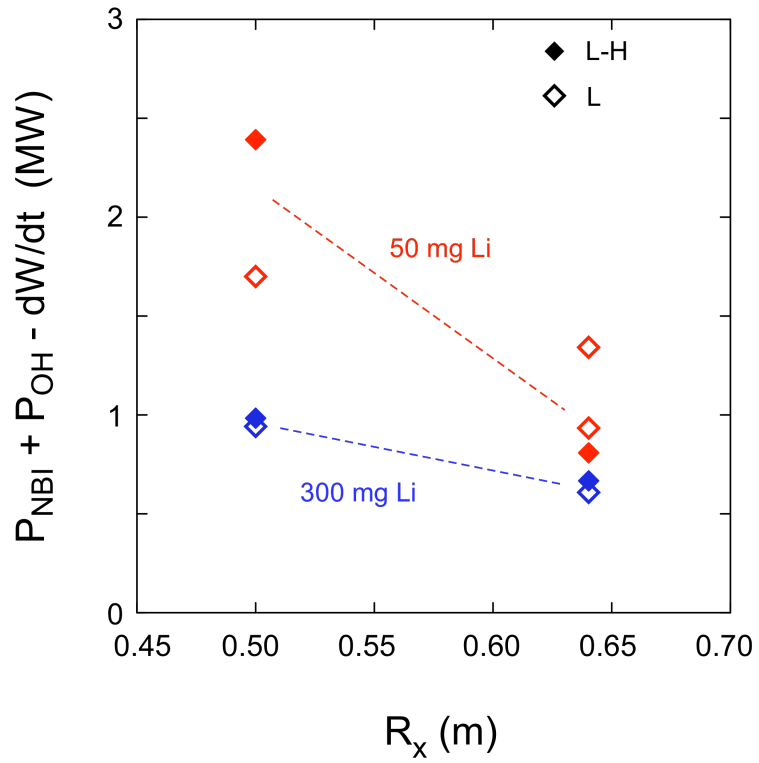


**Figure 12.** The open diamonds are discharges that transitioned into the H-mode, while the filled diamonds are discharges that remained in L-mode for two different lithium deposition rates and as a function of X-point radius, corresponding to different triangularities in NSTX [39].

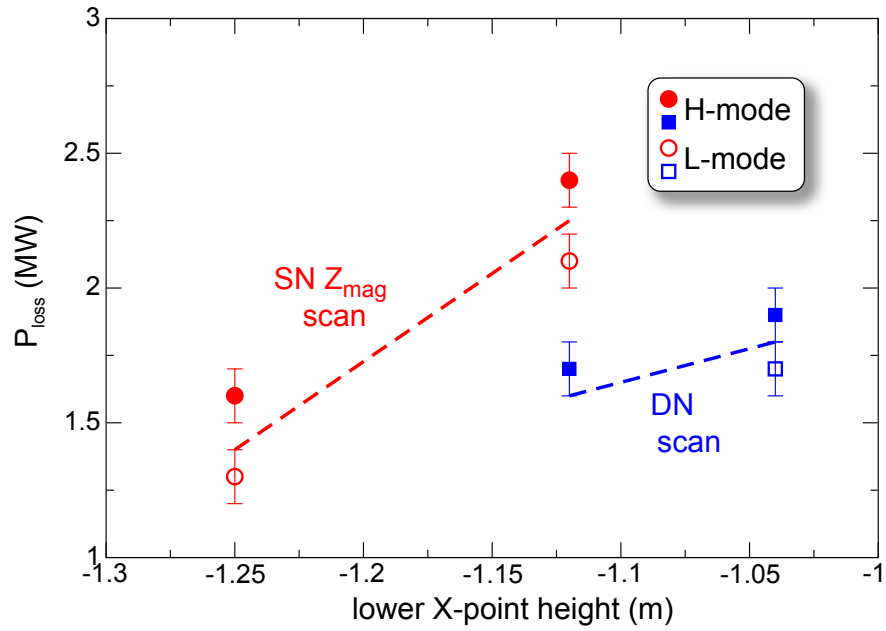


**Figure 13.** Comparison of discharges, which made a transition to H-mode with those that did not, as the location of the X-point was varied in both single-null and double-null MAST discharges [41].

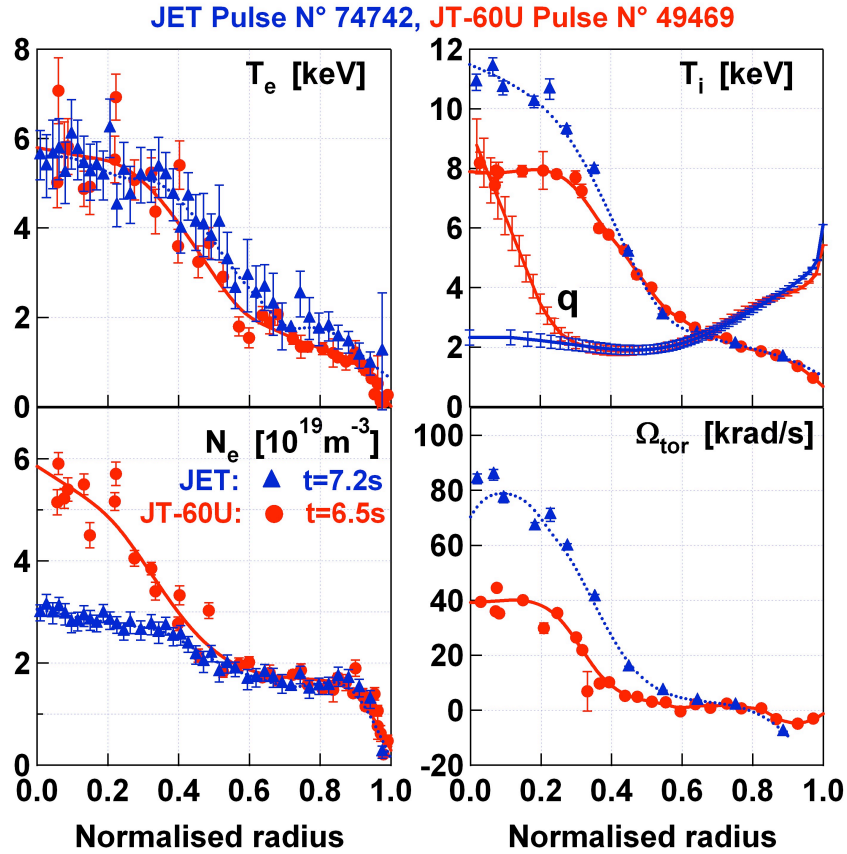


**Figure 14.** Reversed shear experiments with  $q_{\text{min}} \sim 2$  for JET with toroidal field ripple of  $\delta_{\text{TF}}=0.3\%$  (blue) and JT-60U injected torque scan (red.) Profiles are shown at the time of the fully developed ITB phase [47].

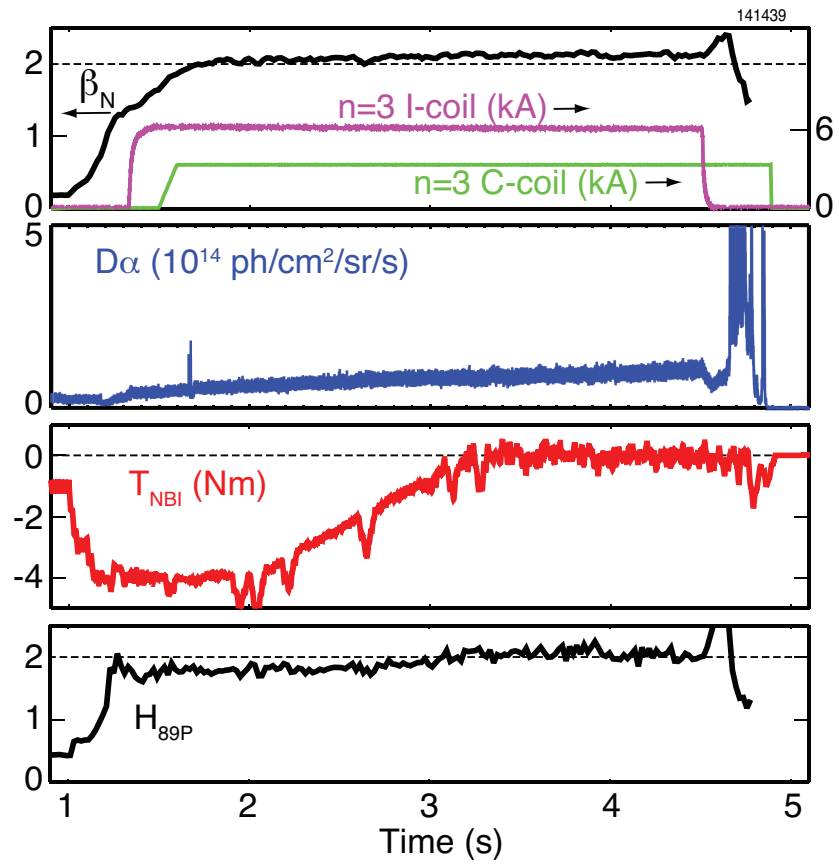


**Figure 15.** The application of non-resonant magnetic fields enables the reduction of neutral beam torque while maintaining the QH mode in DIII-D [51].

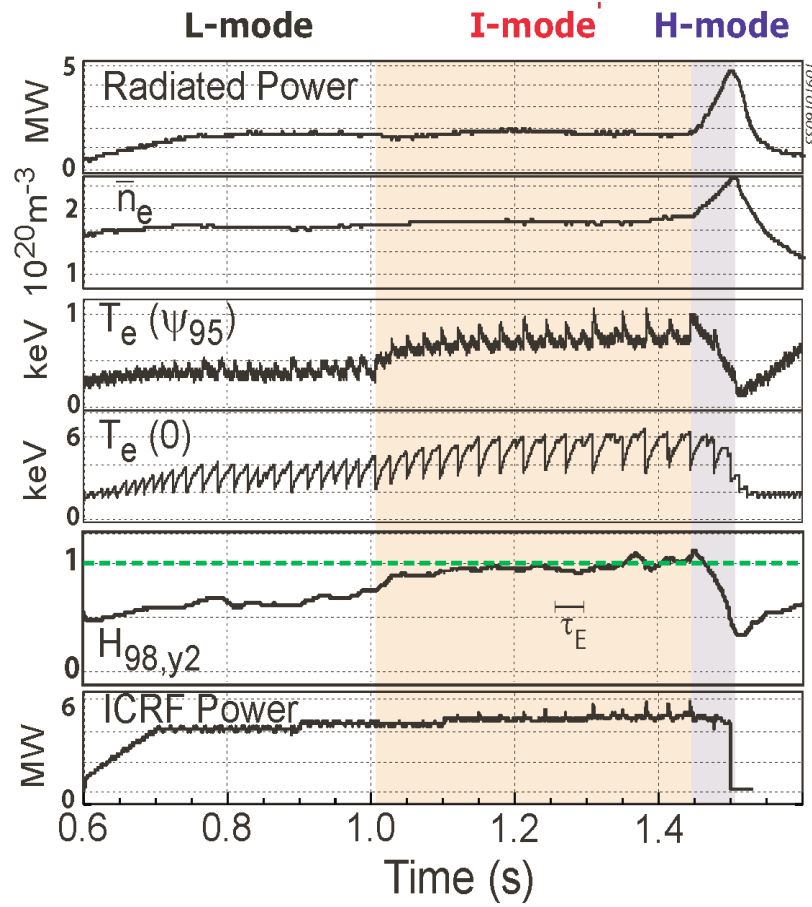


**Figure 16.** Evolution of a C-Mod 1.2MA discharge from L-mode, to I-mode to an ELM-free H-mode. Note at the transition from L-mode to I-mode the edge temperature and energy confinement time increases, in the transition to the H-mode the particle confinement increases resulting in increased radiation [52], reprinted with courtesy of IOP [53].

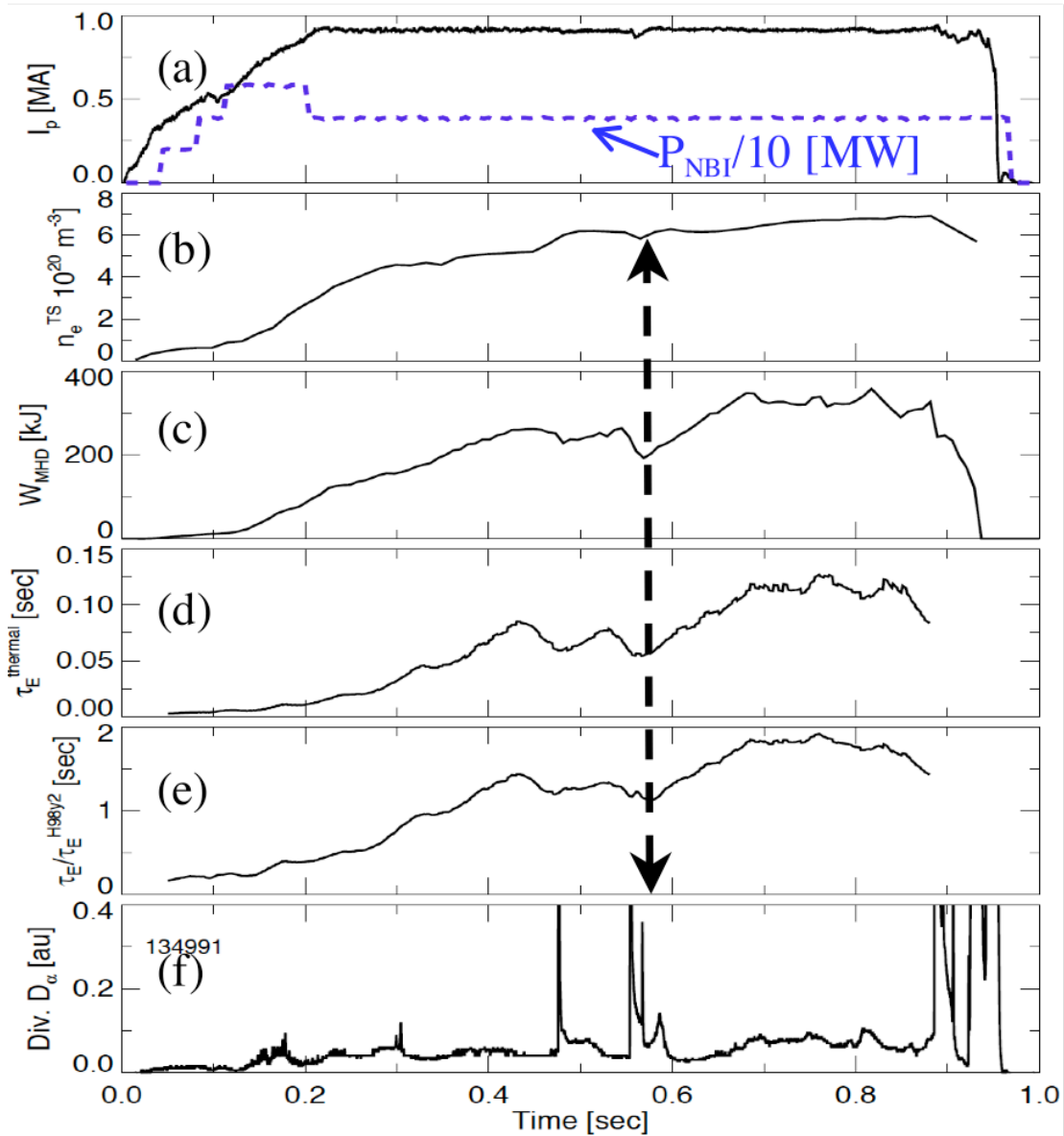


**Figure 17.** Time evolution of NSTX discharge with transition to the enhanced pedestal H mode using lithium coatings: (a)  $I_p$  and NBI power,  $P_{\text{NBI}}$  (dashed), (b) line-average density from Thomson scattering, (c) magnetic measurement of stored energy, (d) energy confinement time, (e) energy confinement time, normalized by ITER98y2 H mode scaling, and (f) divertor  $D_\alpha$  emission. The H mode to EP H-mode transition is indicated by an arrow.[55, permission requested from [59].

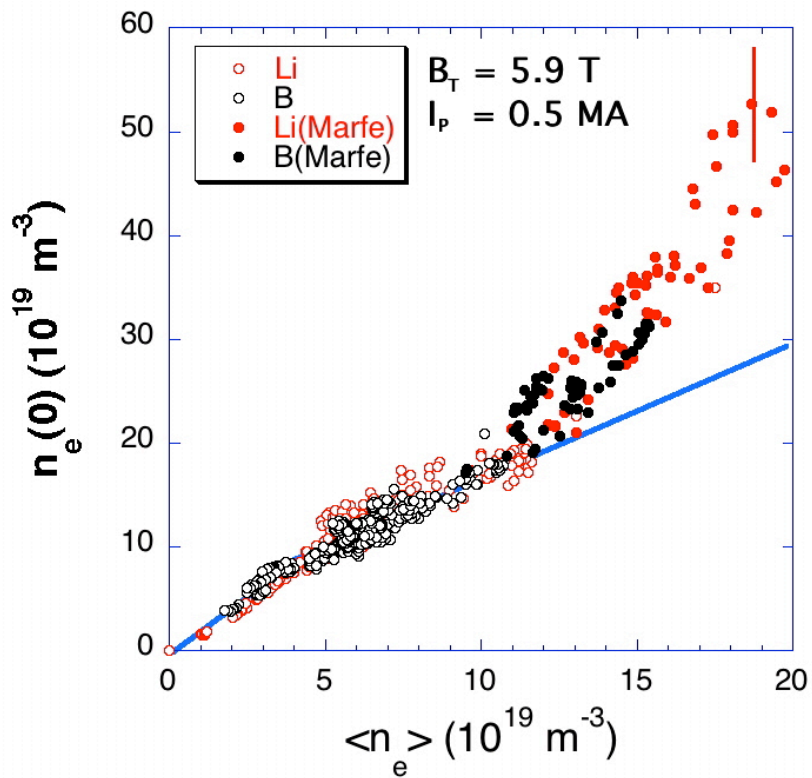


**Figure 18.** Central density versus the volume averaged density, at low field and current in FTU. Red circles are used for lithium and black circles for boron conditioning discharges. Full symbols refer to discharges with well developed a MARFE [56].

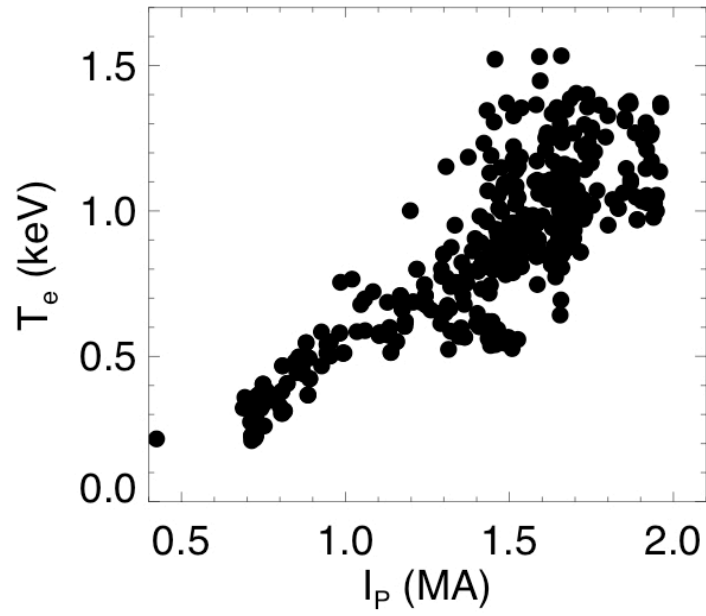


**Figure 19.** Core electron temperature as a function of plasma current in RFX [57].

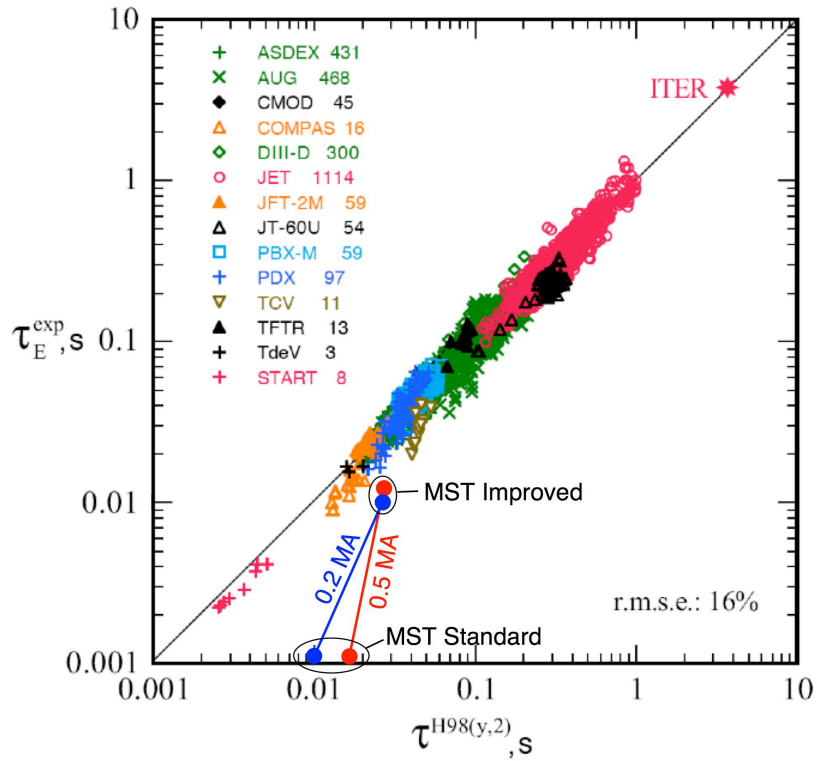


**Figure 20.** MST confinement compared with a ‘fiducial’ tokamak specified by the IPB98(y,2) ELMy-H mode empirical scaling (reprinted from ITER Physics Guidelines, ITER report N 19 FDR 1 01-07-13 R 0.1). Reprinted with courtesy of IOP [63].

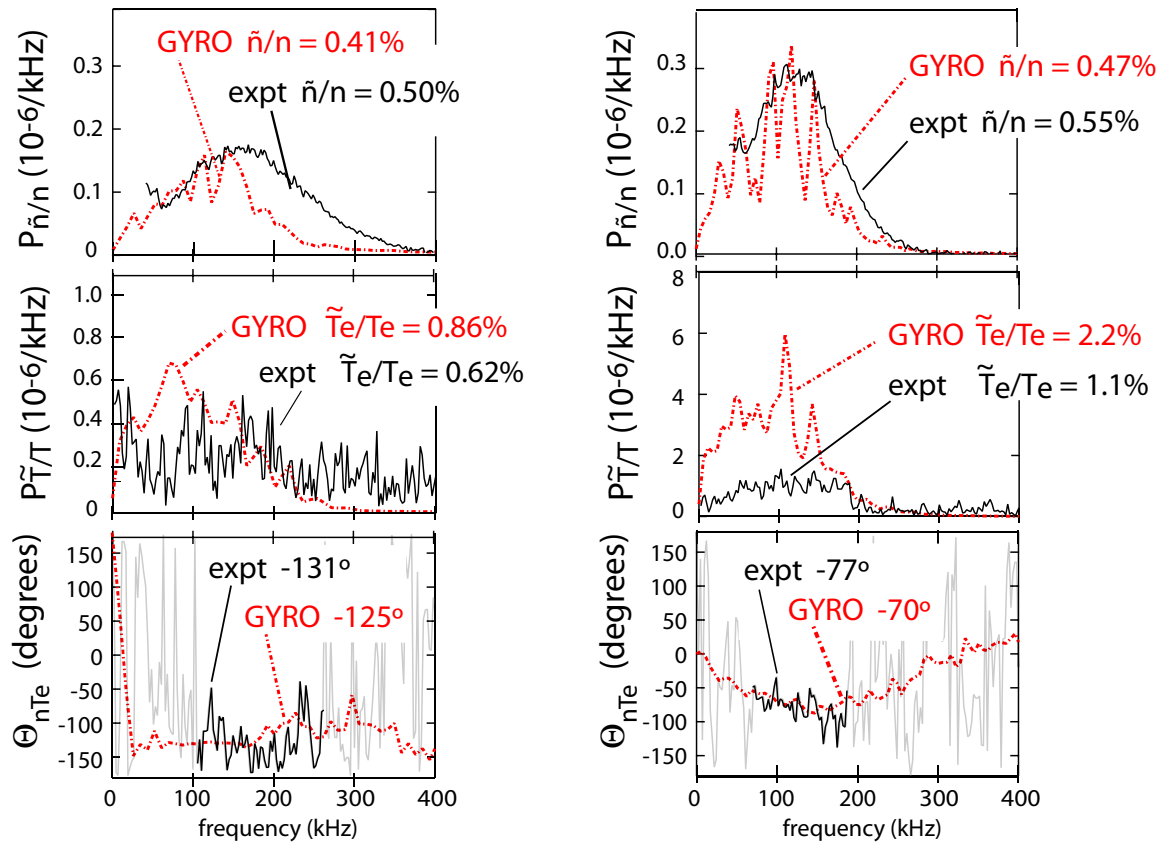


**Figure 21.** DIII-D measurements of electron density, temperature and cross-phase fluctuations are compared with GYRO calculations in which the ratio of  $T_e/T_i$  was changed by the application of ECH. The case in the left hand column has a low  $T_e/T_i$  ratio relative to the case in the right hand column [66].

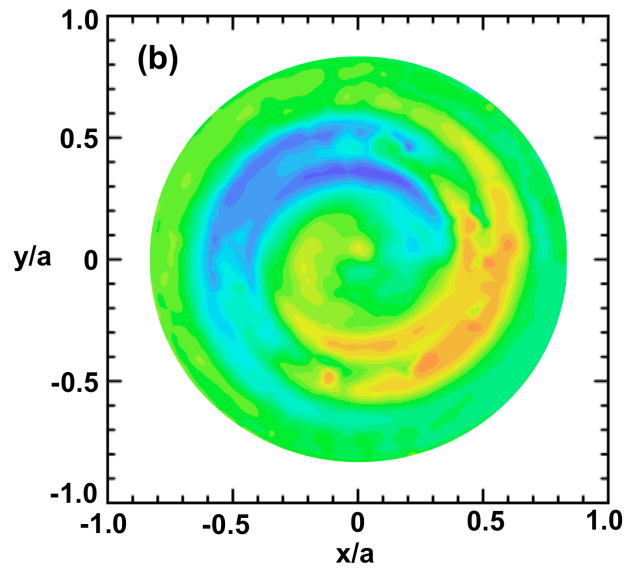
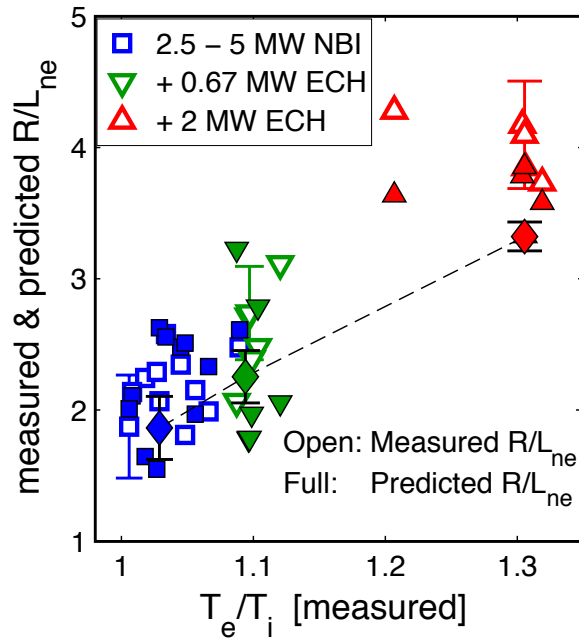
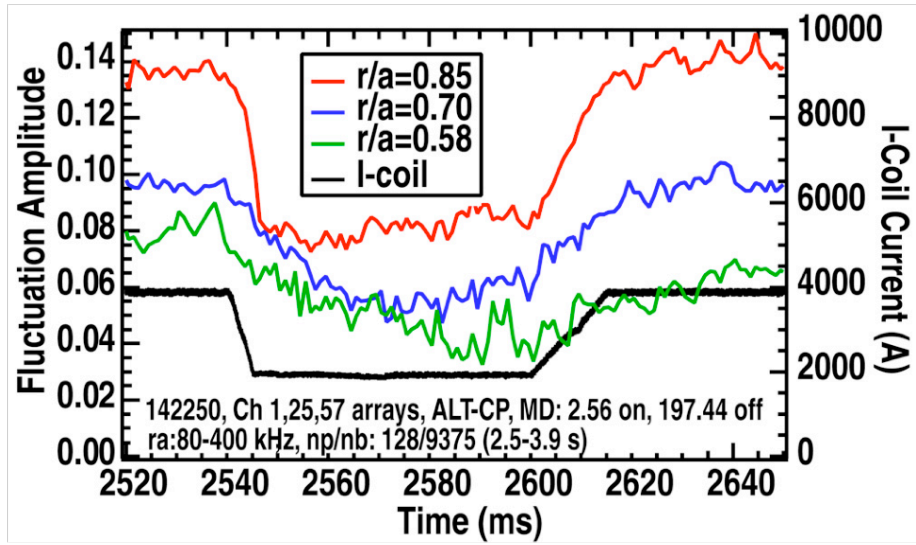


Fig. 22 Reconstructed image of the structure of the temperature fluctuations in LHD where “a” is the plasma minor radius [70].



**Figure 23.** Analysis of three heating phases at half radius in AUG: blue open points correspond to 2.5-5 MW NBI, green to 0.67 MW of ECH and red to +2MW ECH Comparison of predicted quasi-linear GS2 (full symbols with squares, triangles pointing down and up), nonlinear GYRO (diamonds connected by a dashed line) and measured (open symbols) values of  $R/L_{ne}$  as a function of the temperature ratio  $T_e/T_i$  [72].



**Figure 24.** Time resolved beam emission spectroscopy density fluctuations in DIII-D at three radii, and modulated I-coil current [74].

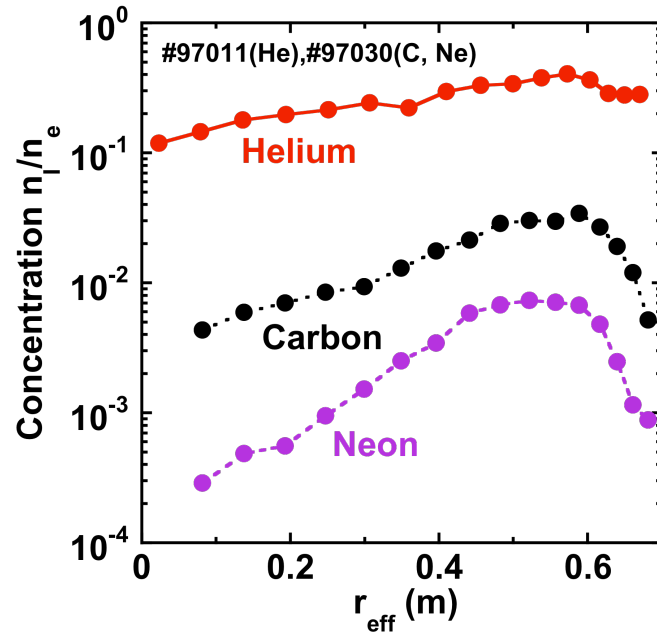
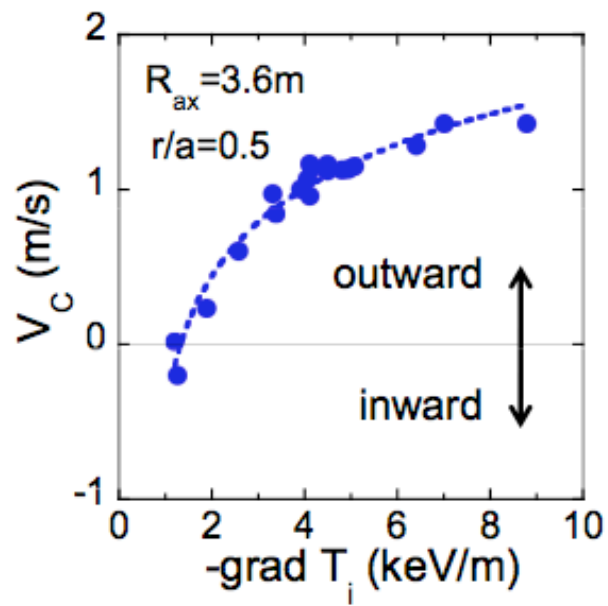
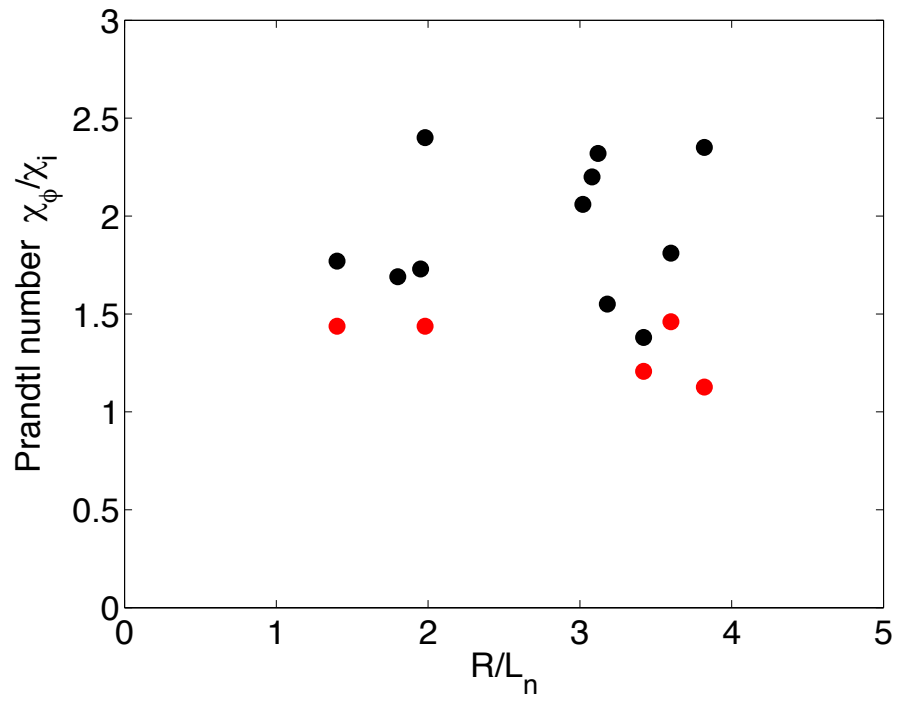


Figure 25. Helium, carbon and neon concentration profiles in LHD [76].



**Figure 26.** Radial impurity velocity as a function of ion temperature gradients in LHD [76].



**Figure 27.** Comparison of JET experimental measurements in black of the Prandtl number versus  $R/L_n$ , with GS2 calculations in red [80].

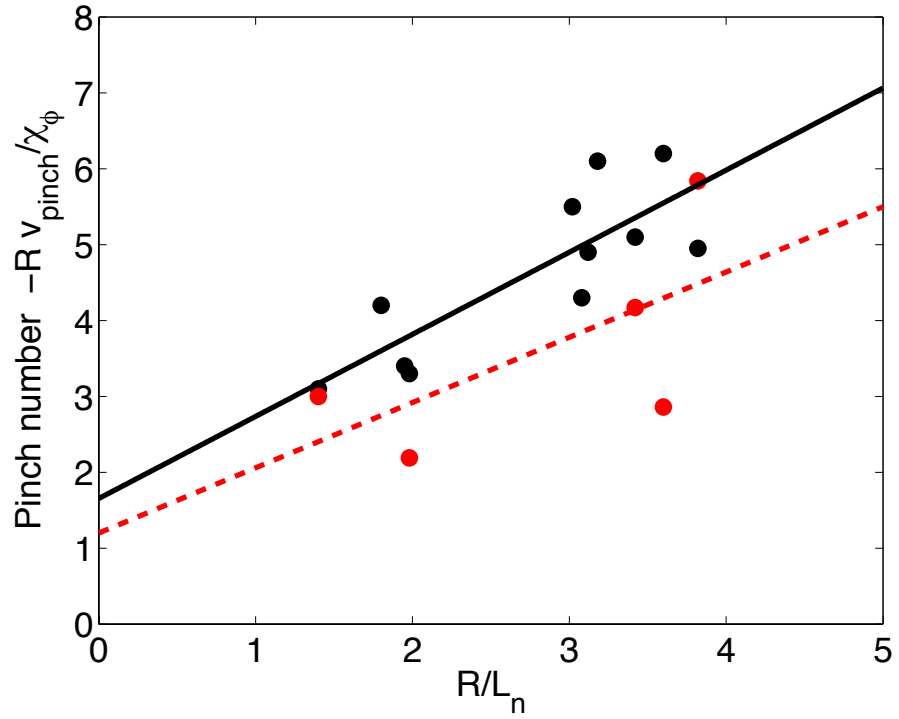


**Figure 28.** Comparison of JET experimental measurements in black of the of the pinch parameter,  $R v_{\text{pinch}}/\chi_\phi$ , versus  $R/L_n$ , with GS2 calculations in red [80].

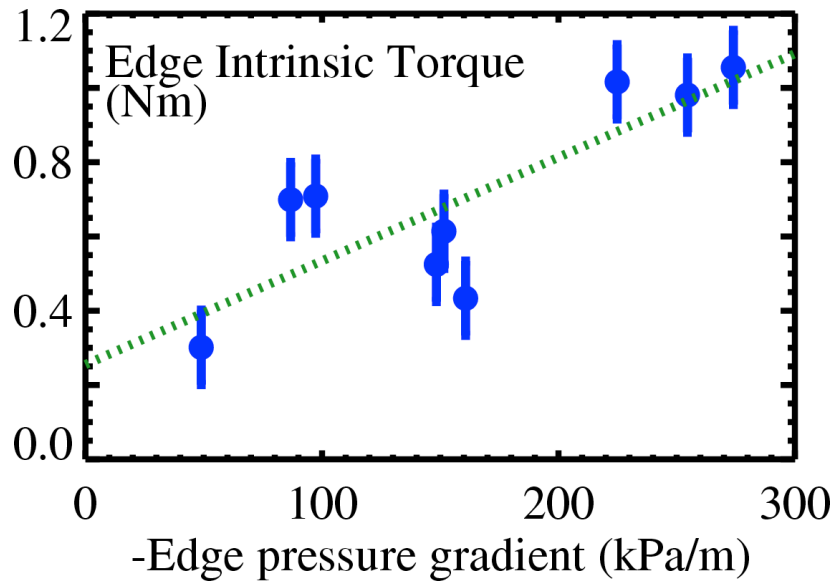


**Figure 29.** The intrinsic torque at the edge of the plasma shows a strong correlation with the edge pressure gradient in DIII-D [82].

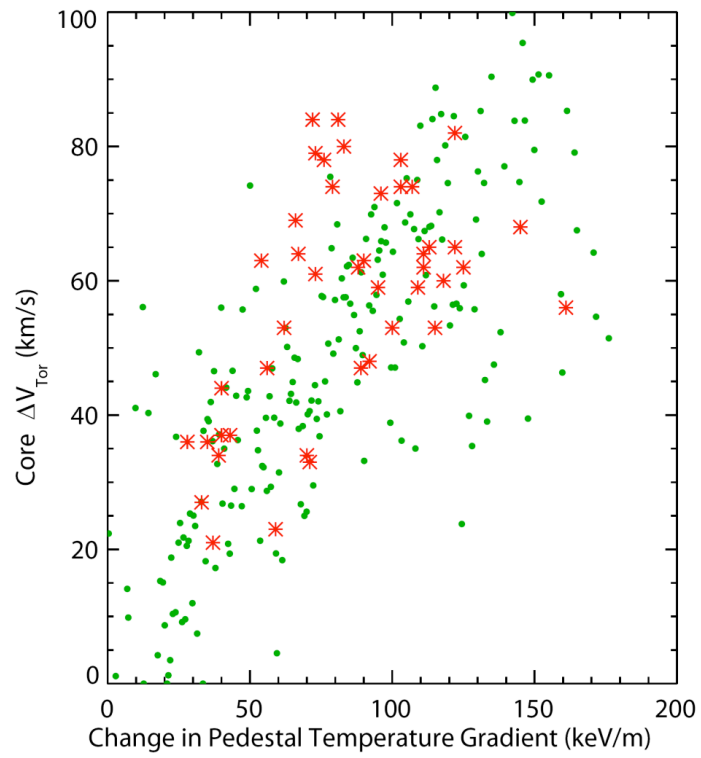


**Figure 30.** The change in the core rotation velocity as a function of the change in the pedestal electron temperature gradient for H-mode (green dots) and I-mode (red asterisks) plasmas in C-Mod [83].

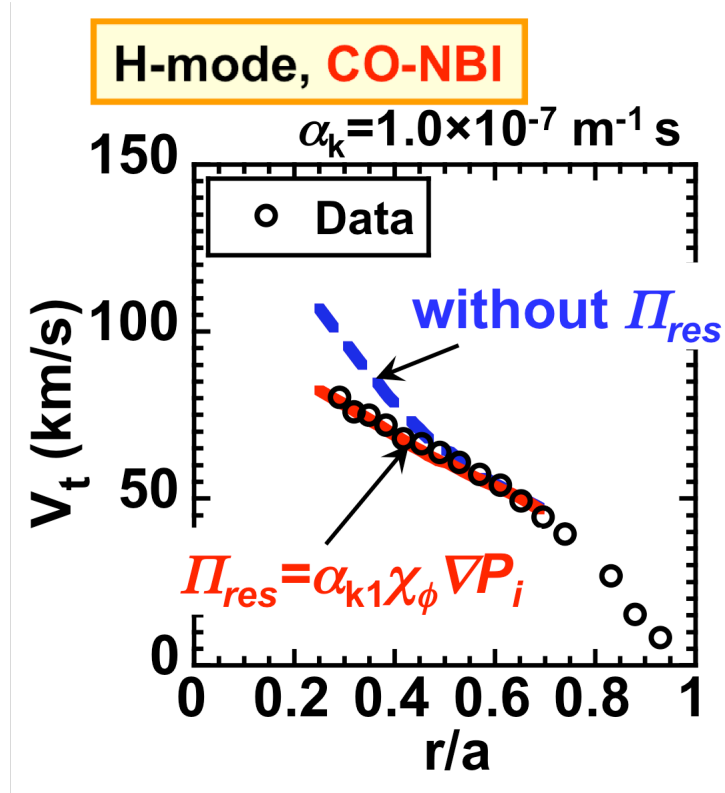


**Figure 31** Profiles of the measured the toroidal velocity,  $V_t$ , compared with the calculated values with  $\Pi_{res} = \alpha_{k1} \chi_{\phi} \nabla P_i$  and without  $\Pi_{res}$  in co-rotating H-mode plasma in JT-60U[84].

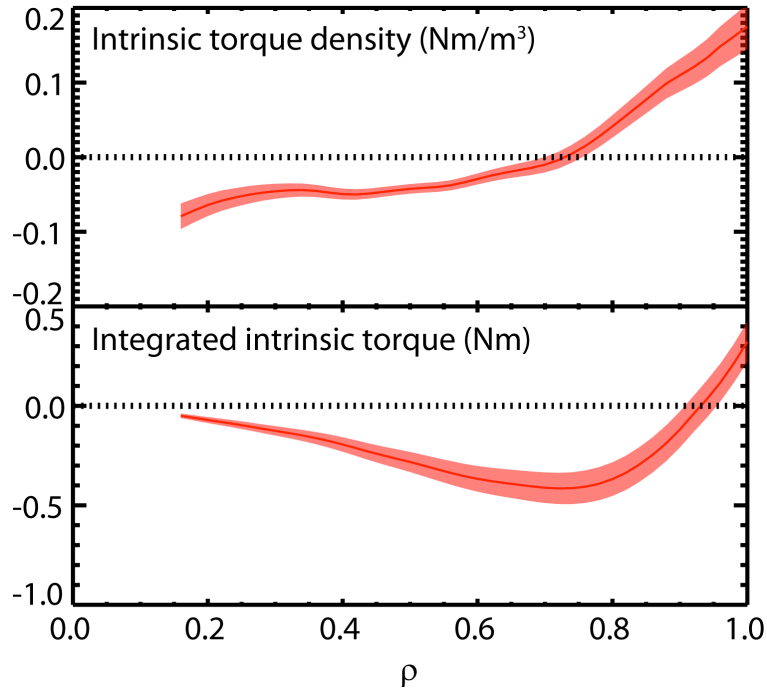


**Figure 32.** (a) H-mode intrinsic torque profile indicates typical H-mode edge intrinsic drive, but with an extended radial region of counter intrinsic torque throughout the core. (b) Integrated intrinsic torque [82].

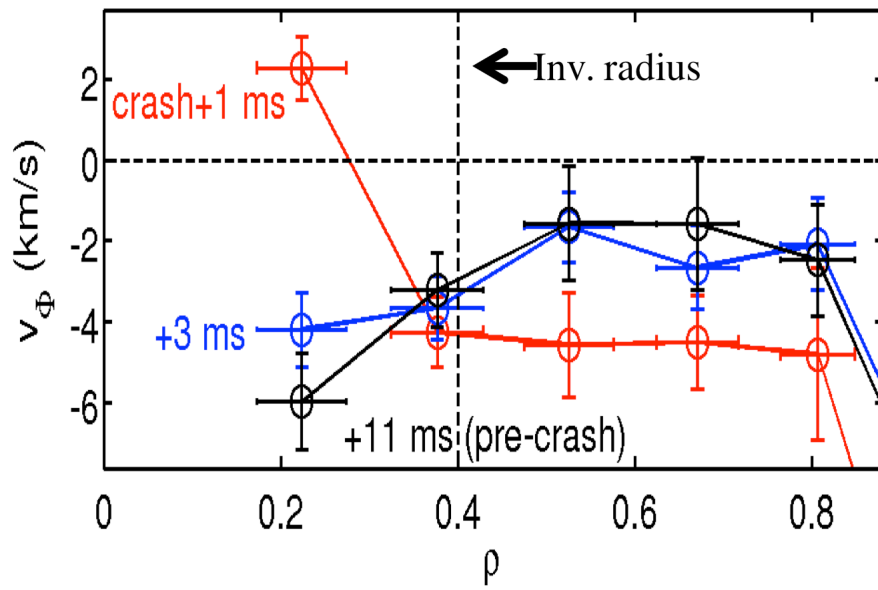


**Figure 33.** The toroidal rotation profile at 1, 5, 3 and 11ms after the sawtooth crash in TCV [88].

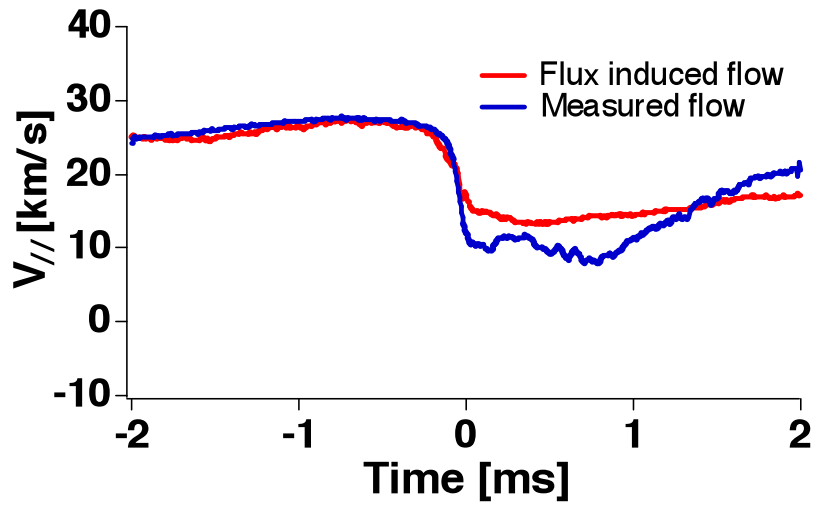


**Figure 34.** Time integrated flux divergence (red line) and ion parallel flow (blue line) are compared in MST following a sawtooth event. Flow at  $t = -0.5$  ms is taken as an integral constant [89].

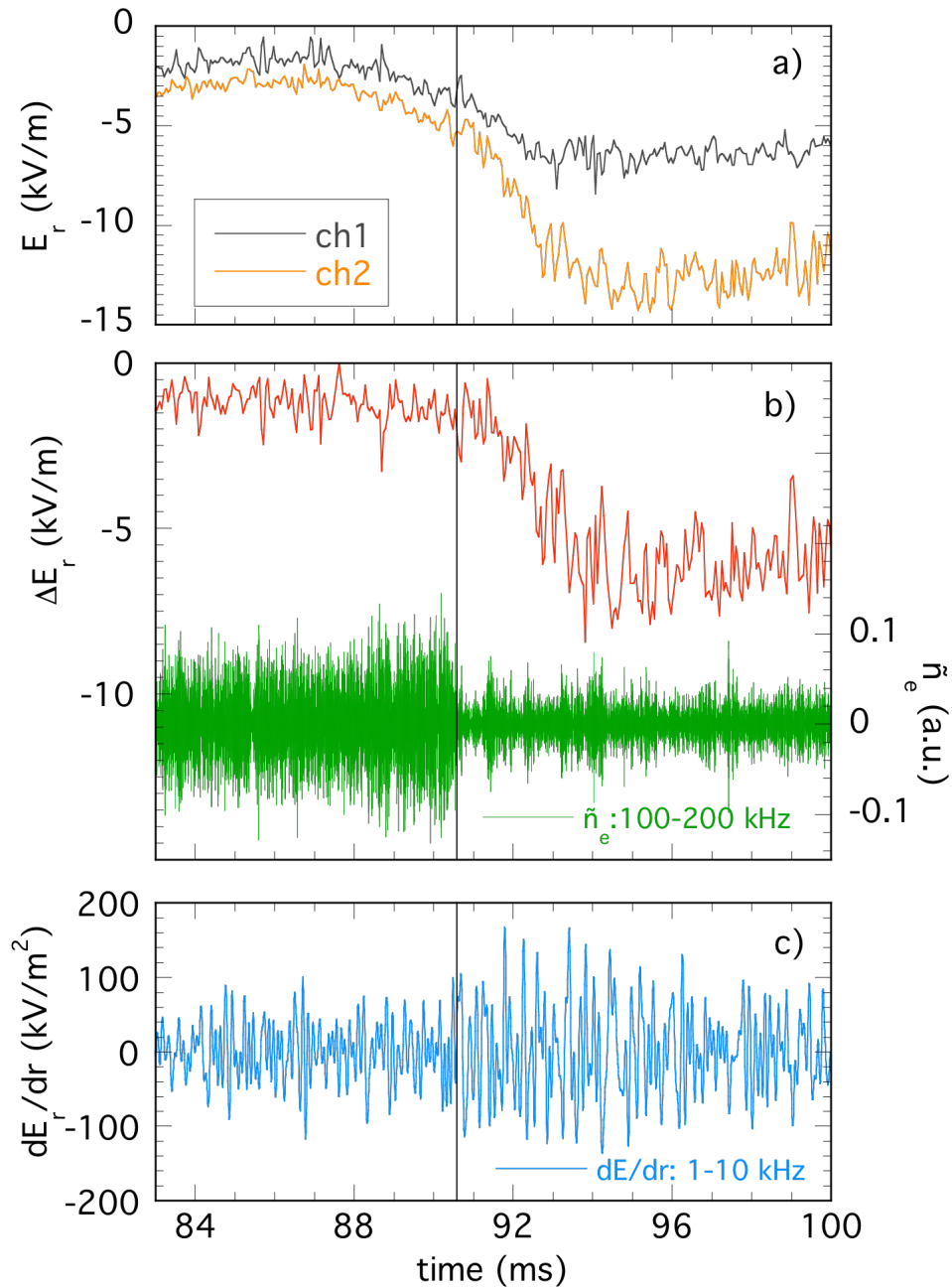


**Figure 35.** Time evolution of the radial electric field in TJ-II at two adjacent radial positions (a), their difference and the high frequency density fluctuations (b) and the low frequency fluctuations in the radial electric field shear (c); plasma heated by both NBIs (900 kW port-through) in the standard configuration  $\iota(a) = 1.65$ . The vertical line indicates the L–H transition time [90, reprinted with courtesy of IOP [91].

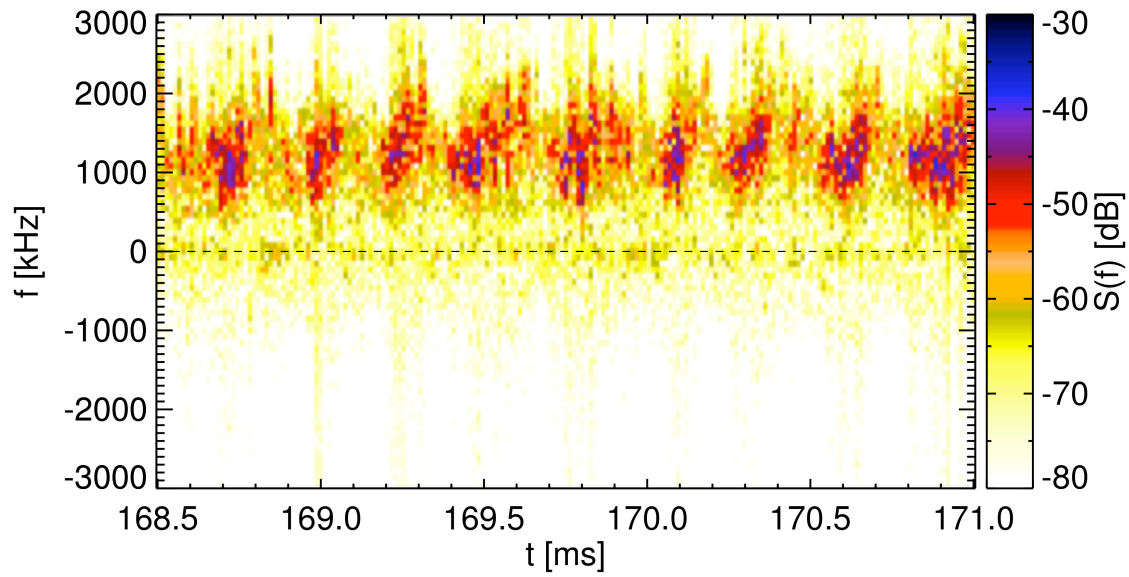


**Figure 36.** Spectrogram of the Doppler reflectometer signal measured at  $\rho \approx 0.8$ , in a magnetic configuration with  $\nu/2\pi = 1.53$  at the plasma edge. The color code reflects the density fluctuation level and the frequency of the Doppler peak gives  $E_r$  [90], reprinted with courtesy of IOP [92].

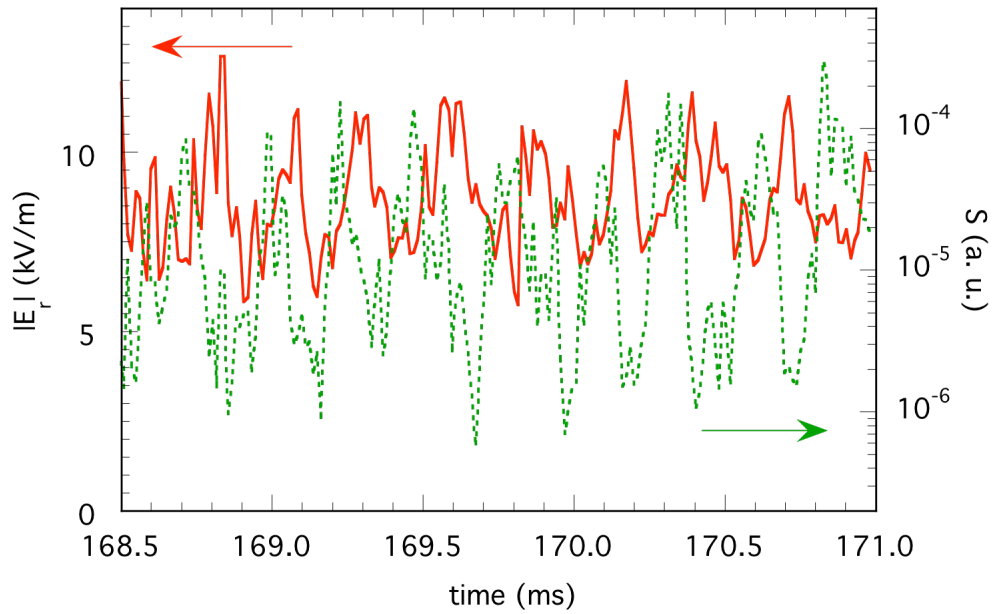


**Figure 37.** Time evolution of  $E_r$  and density fluctuation level obtained from the spectrogram shown in figure 36 [90], reprinted with courtesy of IOP [92].

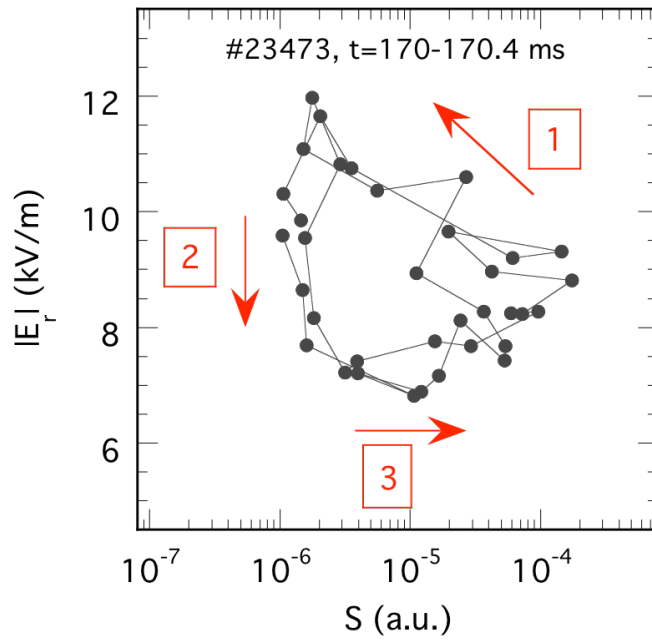


**Figure 38.** Relation between  $E_r$  and density fluctuation level. Only two of the cycles shown in figure 37 are displayed. The time interval between consecutive points is  $12.8 \mu\text{s}$ . [90], reprinted with courtesy of IOP [92].

### Coexistence GAM dominant

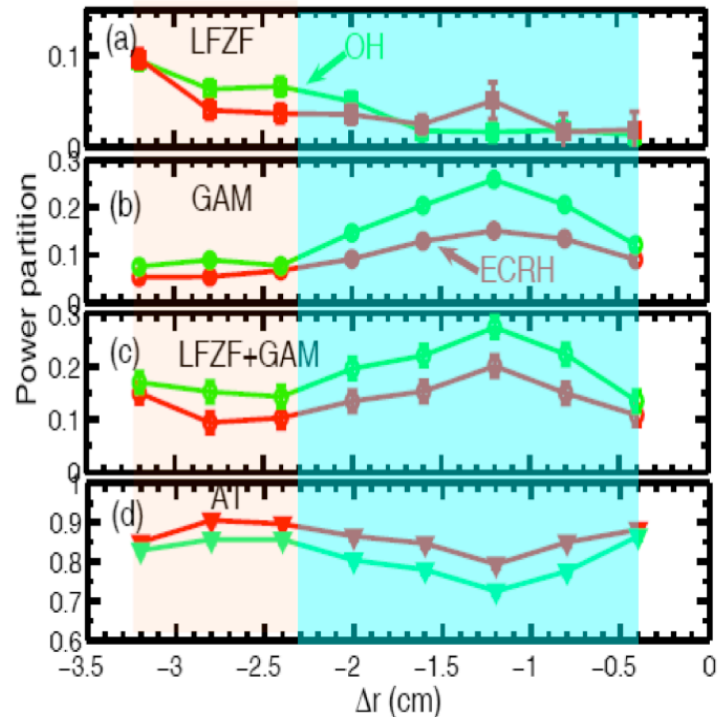


**Figure 39.** The radial distributions power fraction in Ohmic and ECRH plasmas in HL-2A: (a) low frequency zonal flows (LFZF), (b) geodesic acoustic modes (GAM), (c) LFZF+GAM and (d) ambient turbulence (AT) [94].

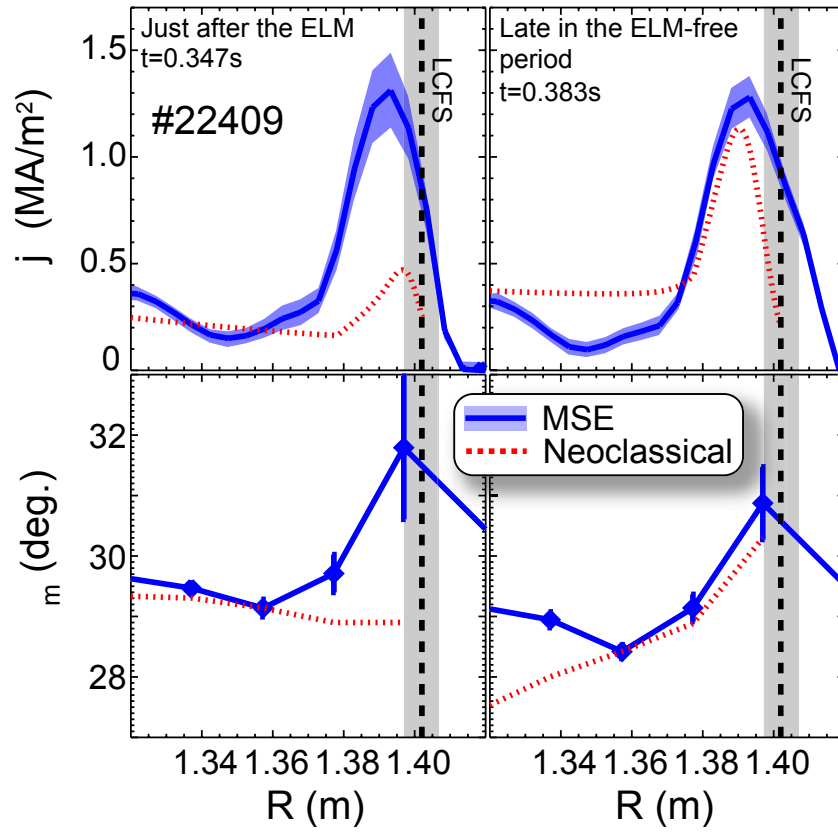


**Figure 40.** Comparison of  $j_\phi$  from MSE measurements with neoclassical calculations [41].

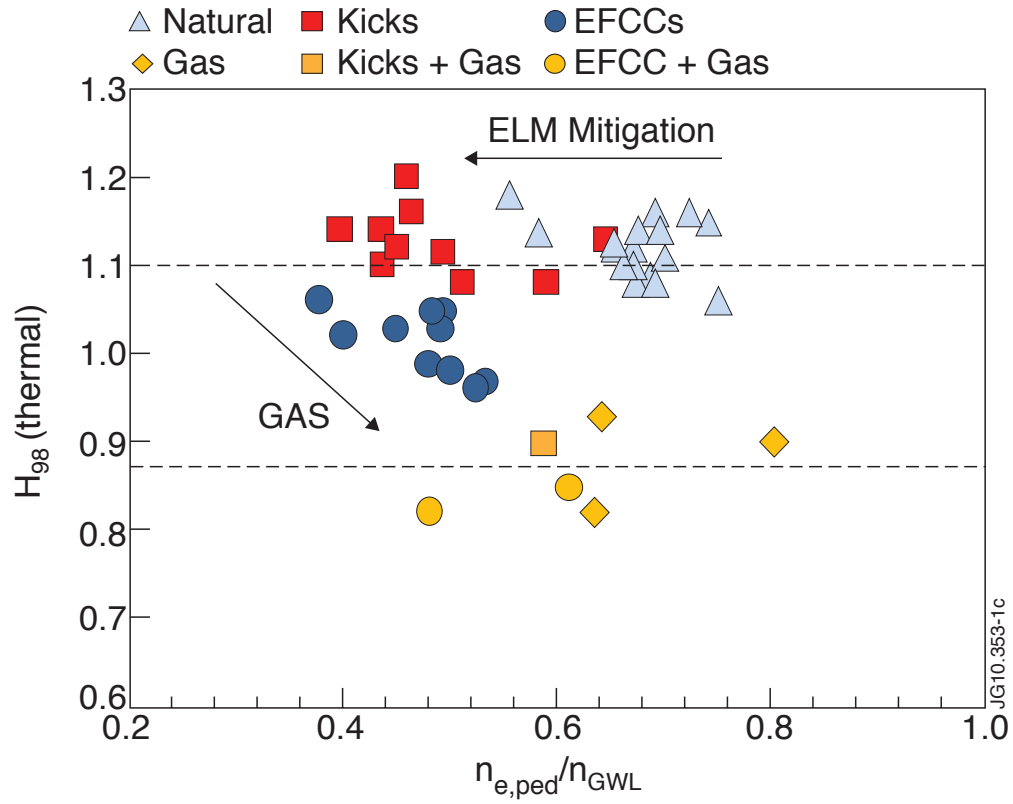


**Figure 41.** Energy confinement enhancement factor  $H_{98}$  vs. pedestal density normalized to Greenwald density for different ELM mitigation techniques [29].

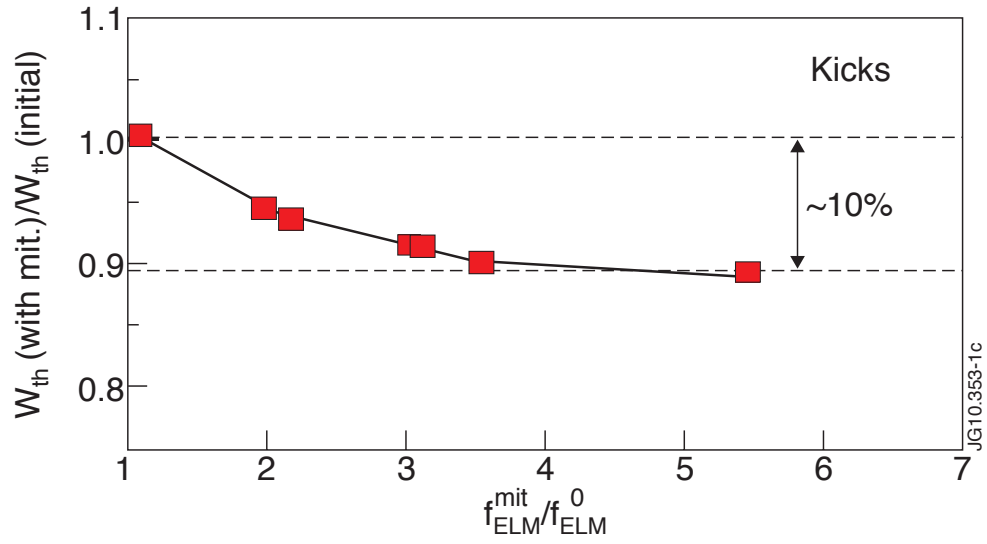


**Figure 42.** Ratio between the thermal stored energy during and before the application of vertical kicks with the increase in ELM frequency [29].



---

# Princeton Plasma Physics Laboratory Office of Reports and Publications

Managed by  
Princeton University

under contract with the  
U.S. Department of Energy  
(DE-AC02-09CH11466)

---

P.O. Box 451, Princeton, NJ 08543  
Phone: 609-243-2245  
Fax: 609-243-2751

E-mail: [publications@pppl.gov](mailto:publications@pppl.gov)

Website: <http://www.pppl.gov>